Is manganese the key? Lowering the dolomite kinetic barrier via redox-driven templating

Daniel A. Petrash[1,2], Astolfo Valero[2], Or M. Bialik[3,4], Yihang Fang[5], Maartje Hamers[6], Travis B. Meador[2,7], Tomaso R.R. Bontognali[8,9,10] Michael Ernst Böttcher[11,12,13] & Oliver Plümper[6,14]

[1] Czech Geological Survey, Prague, Czech Republic, daniel.petras@geology.cz

[2] Greifces, Czech Republic

[3] University of Münster, Germany

[4] Israel Oceanographic and Limnological Research, Israel

[5] University of Missouri–Kansas City, USA

[6] Utrecht University, The Netherlands

[7] University of South Bohemia, Ceske Budejovice, Czech Republic

[8] Space Exploration Institute, Switzerland

[9] University of Basel, Switzerland

[10] Environmental Science Centre, Qatar, Qatar

[11] University of Greifswald, Germany

[12] University of Rostock, Germany

[13] Leibniz Institute for Baltic Sea Research, Germany

[14] University of Bremen, Germany

Abstract

Fabric-preserving and strata-bound dolostones in deep-time successions defy high temperature burial models, implying an elusive low-temperature, syndepositional formation pathway. Here, we demonstrate a kinetically facile route to disordered dolomite nucleation driven by the synergy of manganese redox cycling and carboxyl functionalization. Using a bio-inspired electrochemical reactor, we show that electrochemical valence state manganese modulation accelerates Mn sequestration into authigenic carbonate by 61% (*vs*. <25% in non-electrochemical control) and enhances Mg^{2+} and Ca^{2+} co-incorporation in polycrystalline precursor by ~52% relative to control. The crystallization route generates reactive, electrode surface-confined Mn(III) intermediates where carboxyl ligand stabilization suppresses oxide precipitation, enabling the rapid nucleation of spheroidal magnesian kutnahorite. Nanostructural characterization reveals a core-shell architecture where this isostructural precursor templates the epitaxial growth of substitutionally disordered dolomite cortices on the spheroidal aggregates. Mechanistically, localized acidity from redox cycling triggers a "proton-driven cation pump," actively mobilizing Mg^{2+} from the functionalized hydrogel reservoir to the mineralization front near the electrode interface. Mg^{2+} incorporates into lattice-distorted sites previously occupied by Mn^{2+} in the templating phase. This electrochemical mechanism can be extrapolated to explain the paragenesis of delicate fabric-retentive dolostones in deep time.

1. Introduction

The dolomite conundrum persists as a paradox in sedimentary geochemistry, contrasting the punctuated abundance of dolomite in pre-Mesozoic strata—where it served as a major carbon and magnesium sink (Berner, 1991), with its scarcity in modern shallow-marine environments (McKenzie, 1991; Holland and Zimmerman, 2000). At the heart of this paradox lies a profound

kinetic barrier, i.e., the synthesis of ordered dolomite ($CaMg(CO_3)_2$) remains intractable at low temperatures (<80°C).

Despite being thermodynamically favored in marine-derived fluids (Wigley, 1973; Given and Wilkinson, 1987; Wilkinson and Algeo, 1989), the formation of the enigmatic mineral is inhibited by the high enthalpy of dehydration of the Mg^{2+} ion (Lippmann, 1973; Hardie, 1987). Mg has a high charge density and binds water molecules into a rigid hydration shell with slow exchange rates (Lippmann, 1973; Maguire & Cowan, 2002; Helm & Merbach, 2005). Additional kinetic barriers include the difficulty of achieving cation-ordering, which requires geological timescales at low temperature (Kell-Duivestein et al., 2019; Pina et al., 2022), and high nucleation energy, which favours disordered precursors that require protracted aging to form ordered dolomite (Meister et al., 2023).

Early high-temperature (≥150°C) experiments established protodolomite as a compulsory precursor that can lead to dolomite (*sensu stricto*) via dissolution-reprecipitation and recrystallization (Graf and Goldsmith, 1956; Bischoff 1968; Katz & Matthews, 1977; see also Kaczmarek & Sibley, 2014; Rodriguez-Blanco et al., 2015; Kaczmarek & Thornton, 2017). However, these kinetic often models fail to explain the massive, fabric-retentive dolostones and fabric-selective patterns (e.g., Aljinović et al., 2025; Gingras et al., 2004). Consequently, low-temperature mechanisms involving microbial agents are frequently invoked (Petrash et al., 2017).

Subsurface microbes can overcome kinetic barriers twofold: (i) by modulating local supersaturation via metabolic alkalinity generation; and (ii) by producing extracellular polymeric substances (EPS) that lower Mg-dehydration energy and template nucleation (Trichet and Défarge, 1995; Wang et al., 2009; Bontognali et al., 2010, 2014; Zhang et al., 2012a; Roberts et al., 2013; Petrash et al., 2017). While laboratory timescales preclude observing the development of cation ordering in microbial synthetic precipitates formed at low

78 temperature (Kell-Duivestein et al., 2019; Pina et al., 2022), microbial activity demonstrably
79 yields the requisite Mg-Ca rich precursors (Al Disi et al., 2021).

80 Complementary to direct microbial mediation, various catalysts appear to facilitate
81 reaction kinetics. These include: (i) organic solvents (Oomori and Kitano, 1987; Fang et al.,
82 2022) simulating hydrophobic EPS domains (Zhang et al., 2012a); (ii) dissolved silica (Fang
83 and Xu, 2022; Al Disi et al., 2024); (iii) sulfide (Zhang et al., 2012b); (iv) ammonia (Slaughter
84 and Hill, 1991; Meng et al., 2024; Petrash et al., 2025); and (v) zinc (Vandeginste et al., 2019).
85 Among these agents, manganese (Mn) distinguishes itself through a multi-modal capacity to
86 drive dolomite formation via redox-controlled alkalinity (Petrash et al., 2015), templating
87 (Daye et al., 2019), and lattice distortion (Han et al., 2024).

88 Dolomite establishes a solid solution series with ankerite ($CaFe(CO_3)_2$) and kutnahorite
89 ($CaMn(CO_3)_2$) via continuous substitution at the Mg-site. The pure ferroan end-member is
90 unstable, meaning natural ankerite invariably retains Mg, whereas stoichiometric kutnahorite
91 naturally exists but is rare (Frondel and Bauer, 1955; Peacor et al., 1987). Instead, it typically
92 manifests as metastable disordered kutnahorite with variable Ca:Mn ratios (Peacor et al., 1987;
93 Mucci, 1991, 2004; Polgári et al., 2007). The intermediate composition phase exhibit
94 substantial preferential substitution of Mg at the Mn-sites and can be expected to form as a
95 metastable authigenic mineral (Peacor et al., 1987).

96 We hypothesize that metastable disordered kutnahorite can serve as the critical kinetic
97 bridge for dolomite formation. If Mn^{2+} forms a precursor double carbonate structure analogous
98 to dolomite (Peacor et al., 1987) but with lower kinetic barriers, then the distorted lattice
99 structure of this precursory, intermediate phase may act as an epitaxial scaffold, lowering the
100 activation energy for subsequent Mg^{2+} incorporation into an isostructural lattice. We propose
101 that cyclic redox oscillations—specifically involving transient Mn(III) regeneration— can
102 drive the heterogeneous nucleation of dolomite on kutnahorite surfaces. To validate this

mechanism, we implemented a pH-stat synthesis coupled with electrochemical cycling in the presence of carboxylated ligands (alginate). This experimental design mimics a carboxyl-rich biofilm matrix subject to dynamic redox potentials, effectively reproducing the fluctuating microenvironments characteristic of the natural settings where authigenic dolomite forms (Petrash et al., 2015; McCormack 2018, 2024; Han et al., 2024). By identifying a kinetically facile route wherein a kutnahorite template circumvents the kinetic barriers to dolomite formation, this study provides a reproducible mechanism for further investigating non-equilibrium double-carbonate formation and advances a predictive paragenetic framework for evaluating dolomite abundance in deep time.

2. Methods

2.1 Precipitation setup

The experimental design comprises a H-cell electrochemical system (150 mL borosilicate glass reaction vessels) connected to an automatic titrator (SI Analytics Titroline 7000). The electrochemical system was filled with 125 mL of 80 mM $NaHCO_3$ electrolyte solution and it cells were separated by an anion exchange membrane (Fumasep® FKE-50, Fumatech GmbH); and were continuously stirred at 250 rpm via synchronized MIXDrive stirrers (2Mag). One cell was open through a 0.2 μm cellulose acetate filter to maintain the dissolved inorganic carbon of our electrolyte in equilibrium with the atmosphere at 25°C. The headspace of the other cell was kept anoxic by a constant flow of argon, initiated 5 min before experiments. In the anoxic cell, a graphite rod working electrode (WE, CP-2200, CP-Graphitprodukte GmbH) and an Ag/AgCl reference electrode (sat. KCl, +197 mV *vs.* standard hydrogen electrode (SHE); RE-1B, ALS Japan) were inserted. In the oxic cell, another graphite rod was used as the counter electrode (CE). A schematic representation of the electrochemical system is shown in Figure 1.

To investigate the influence of carboxyl functionalization, to a set of experiments we added to the electrolyte Na-alginate (300 $mg \cdot L^{-1}$, Sigma-Aldrich)—a commercially available compound composed exclusively of carboxyl functional groups. Alginate is key component of EPS in microbial mats colonizing hypersaline, dolomite-forming settings (Petrash et al., 2011). At the environmentally relevant pH range (i.e., >p*K*a) alginate is crosslinked by metal ions, forming a hydrogel (Petrash et al., 2011). This property can render the resulting hydrogels conductive (e.g., Ji et al., 2022).

To isolate the effects of organic functionalization and electrochemical modulation on mineral formation, four experimental conditions were tested: **(E_{00})** control, lacking both functionalization and electrochemical modulation, served as the baseline for surface precipitation; **(E_{10})** carboxyl-functionalized without electrochemistry, this condition isolated the effect of the carboxyl groups on mineral formation in the absence of an applied potential; **(E_{01})** a non-carboxyl-functionalized sample was subjected to electrochemical modulation to assess the role of redox cycling in the absence of the biopolymer; **(E_{11})** a carboxyl-functionalized surface with an applied electrochemical treatment to evaluate potential synergistic or antagonistic interactions. All conditions were conducted in duplicate.

2.2 Electrochemical precipitation protocol

During each experimental run, an initial pH value of 8.5 ± 0.1 in the anodic cell was raised to 9.1 units after additions of 100 to 200 µL of 0.5 M NaOH solution as pre-titrant. Following pre-titration, a cation-rich feedstock (0.6 M $(Ca,Mg)Cl_2$; Mg:Ca = 6:1) was dosed into the anodic chamber at a rate of 1 mL min^{-1} for 20 minutes (20 mL total); the final working volume of the H-cell setup was 145 mL. The electrolyte pH was maintained at 9.2 ± 0.4 by automatically dosing the titrant into the anodic cell (1.2 to 3.0 mL in total) using the automatic titrator in pH-stat mode. when the value dropped below the experimental pH-envelope.

After the first 5 min of feedstock dosing (*ca*. 5 mL), a single addition of $MnCl_2$ stock solution was added to the anodic cell to achieve a concentration of 10 mM Mn. At this nucleation onset (t = 5 min), the system had reached estimated concentrations of Mg ≈ 21 mM and Ca ≈ 3.6 mM. This established a far-from-equilibrium state—supersaturated with respect to Mg-Ca phases but undersaturated for Mn-precursors (Table S1)—effectively isolating Mn-nucleation to the electrode interface. As feedstock dosing continued to completion (t = 20 min), the background concentrations rose to Mg ≈ 86 mM and Ca ≈ 14 mM, sustaining the high thermodynamic driving force. Deionized water (18.2 $M\Omega \cdot cm^{-1}$) and analytical-grade reagents were used to prepare all solutions. Concurrently with reactant dosing, oscillations in the redox potential of the electrolyte were induced by using a Dropsens μStat 8000 multichannel potentiostat (Metrohm, Spain) in cyclic voltammetry mode (CV) for 28 min. The electric potential was continuously swept between -0.1 and 0.5 V at a scan rate of 2 mV s^{-1}. This environmentally relevant Eh window (e.g., Jørgensen et al., 1979; Di Loreto et al., 2021) targets the Mn(II)/Mn(III) couple, driving oxidative cycling at the periphery of the working electrode (WE) without inducing water hydrolysis or insoluble Mn(IV) oxide precipitation. It aligns with the nitrogenous and manganous zone where incomplete manganese cycling is thermodynamically dominant (Canfield and Thamdrup, 2009). After titration, the electrolyte solution in the anodic cell was left undisturbed for 24 h to permit stabilization of the surface precipitates. Following this step, the WEs were retrieved, disassembled, and stored under anoxic conditions until solid-phase characterization.

2.3 Solution cation concentration determinations

Samples were collected from the anodic chamber at three distinct experimental stages: **(S_i)** immediately before the addition of 10 mM $MnCl_2$—when 5 mL of the $(CaMg)Cl_2$ reactant (further referred here to as cation feedstock) had been added (i.e., $[Ca]_{added}$ = 3.6mM, $[Mg]_{added}$ = 21mM; Mn = 10 mM); **(S_{ii})** following the complete dosing of 20 mL of the cation feedstock

(i.e., $[Ca]_{added}$ = 14mM, $[Mg]_{added}$ = 86 mM, $[Mn]_{added}$ = 10mM); and **(S_{iii})** after the 24 h stabilization period. The working solutions were acidified with trace grade HNO_3 (67% v/v, Sigma-Aldrich). The cations crosslinking alginate are recovered after acidification, and the concentrations of Ca^{2+}, Mg^{2+}, and Mn^{2+} relative to the total analyte added to the system are determined using a triple quadrupole inductively coupled plasma mass spectrometer (ICP-MS; Agilent 8800). Precision was verified against certified standards, and the relative standard deviation was <10% of the reported value for all measurements.

2.4 Multiscale microscopy and nanoscale characterization

Electron-transparent lamellae of surface precipitates were prepared for (scanning) transmission electron microscopy ((S)TEM) using a Helios Nanolab G3 (Thermo Fisher Scientific) focused ion beam scanning electron microscope (FIB-SEM) at the University of Utrecht. This instrument was also employed to assess the micrometre-scale morphological features of the precipitates. Sub-micron scale imaging of lamellae, with thicknesses ranging from 250 to 300 nm, was conducted in bright-field (BF) TEM, dark-field (DF) TEM-EDS, and high-angle annular dark field (HAADF) STEM modes. These were performed using either a Thermo Fisher Talos F200X coupled to a Super-X detection system, or a Spectra 300 instrument, operated at accelerating voltages of 200 kV and 300 kV, respectively. Selected area electron diffraction (SAED) and electron energy loss spectroscopy (EELS) were further utilized in multiple regions of interest to resolve crystallographic and compositional features of the precipitates at the nanoscale. Dual-EELS datasets (core- and low-loss regimes) were acquired using a CCD camera and DigiScan within the Gatan microscopy suite, with a dispersion of 0.15 eV/pixel and a convergence angle of 0 mrad. The low loss spectrum was used to align the core region and evalute the thinknes so gfhe lamella. To estimate the manganese valence state, we employed a combined approach: semi-quantitative background-subtracted white line intensity ratios (L_3/L_2) and the deep-learning spectral decomposition framework MnEdgeNet

(Ji et al., 2023). For the latter, spectra were analyzed using the noise-free model to strictly constrain oxidation states based on peak position and spectral shape. Additionally, energy-dispersive X-ray spectroscopy (EDS) was employed to map the spatial distribution of Mn, Ca, and Mg within sacrificial areas of the precipitates.

3. Results

3.1 Response to titration and electrochemical treatments

Titration data (Fig. 2) show that control samples (E_{00}) required maximal external neutralization due to unbuffered proton release during precipitation. Conversely, potential sweeping alone (E_{01}) reduced titrant demand via cathodic proton consumption (Eq. 1). Conversely, potential sweeping alone (E_{01}) reduced titrant demand via cathodic proton consumption (Eq. 1). In E_{01}, proton-coupled electron transfer partially offsets the release associated with carbonate precipitation, explaining the reduced external titrant demand observed in the electrochemical condition.

$$Mn^{III}(OH)_{org} + e^- + H+ \rightarrow Mn^{II}_{org} + H_2O \quad (1).$$

The carboxyl functionalization alone (E_{10}) provided intrinsic buffering capacity, attributed to carboxyl groups (pKa ~3.5–4.5; e.g., Petrash et al., 2011). At the experimental pH, the carboxyl-rich biopolymer forms a hydrogel upon deprotonation and in the presence of cations. As carbonate mineral nucleates, it pulls CO_3^{2-} from the equilibrium, forcing the deprotonation of HCO_3^-. This locally weakens the bond between metals, M, cross-linking the hydrogel as the crystal growth front, releasing these metals back in solution right at the interface of the growing mineral phase (2).

$$R\text{-}COO\text{-}M\text{-}OOC\text{-}R + H^+ \rightarrow R\text{-}COOH + M^{2+} + {}^-OOC\text{-}R \quad (2).$$

The combined system (E11) achieved maximal pH buffering capacity by synergizing active cathodic reduction with passive hydrogel buffering. This dual mechanism effectively

mitigated the acidification front driven by rapid carbonate nucleation, resulting in minimal titrant consumption during cation feedstock addition (Fig. 2)

3.2 Mn redox features developed during electrochemical carbonate synthesis

CV was used to investigate the electrochemical behavior of Mn in the system. In experiments lacking Na-alginate, the graphite electrode showed negligible faradaic activity within the potential window (-0.1 V to +0.5 V vs. SHE), displaying a non-faradaic capacitive current profile (Fig. 3A). Upon the introduction of Na-alginate, distinct quasi-reversible redox features emerged (Fig. 3B). Accordingly, an anodic peak attributed to the oxidation of Mn(II) → Mn(III) was observed at approximately +0.35 to +0.45 V, with a corresponding cathodic peak for the reduction reaction appearing at ca. +0.30 V during the reverse scan (Fig. 3B). This quasi-reversibility indicates that carboxyl functionalization does not merely lower the activation energy but enables the electrochemical reaction. By acting as inner-sphere ligands, the carboxyl groups near the surface of WEs could facilitate electron transfer that is otherwise kinetically inhibited at the bare graphite interface. Therefore, the presence of the return (cathodic) peak confirms that the surface ligand field stabilizes the highly reactive Mn(III) intermediate.

To also monitor the progression of the surface-mediated reaction in functionalized experiments, we recorded the temporal evolution of the current response. The system exhibited reproducible periodic current oscillations, where each 4’-cycle (corresponding to a full potential sweep) featuring sharp anodic and cathodic spikes (Fig. 3C). The pattern confirms the sustained cyclic oxidation and reduction of manganese bound to the carboxylated hydrogel during the active synthesis stage. The signal intensity displayed a progressive attenuation over time (Fig. 3C), indicating that the electroactive surface area was being systematically passivated by deposition of carbonate on the surface of the electrode, leading to fouling and decreased anodic and cathodic capacity.

250 **3.3. Aqueous composition of the reactive solutions**

251 *3.3.1. Magnesium removal: kinetic enhancement*

252 The bulk of Mg removal initiated after 5 doses of the cation feedstock and the single Mn
253 addition. Therefore, S_i recorded [Mg] below certainty levels. By the end of the reactant
254 dosing and titration stage (S_{ii}), between 8.7 ± 1.1% to 28.0 ± 1.0% Mg^{2+} has been removed
255 from solution; an effect largerly enhanced by the electrochemical treatment (Fig 4A).
256 Removal, however, remained incomplete even after the stabilization time lag (S_{iii}), with 66%
257 to 87% of the total Mg^{2+} added to the system persisting in solution across the disparate
258 conditions tested. Electrochemistry alone (E_{01}) achieved the highest removal rates, surpassing
259 the control (E_{00}) by approximately 20%. Electrochemistry with functionalization (E_{11}) was
260 also effective. However, the total amount of Mg co-precipitated in E_{11} was lower than in the
261 functionalized-only condition (E_{10}). Subsequent removal during stabilization was sluggish,
262 increasing by only 3% to 6% relative to the amount removed by the end of titration (Fig. 4A;
263 Table 1).

264 *3.3.2. Calcium removal: Calcium availability as a rate-limiting factor*

265 Prior to the addition of Mn (S_i), approximately 40% of the total Ca had already been removed
266 from the solution (Fig. 4B). This initial depletion is attributed to a quasi-instantaneous
267 homogeneous nucleation of fine-grained suspended precipitate formed upon dosing the cation-
268 rich feedstock into the electrolyte. Similar rapidly formed phases have been characterized as
269 amorphous (e.g., Purgstaller et al., 2016). Considering Mg^{2+} removal trends via co-
270 precipitation (Fig. 4A), and the extremely low Mg distribution coefficient between amorphous
271 calcium carbonates (ACC) and the parental solution (Purgstaller et al., 2019), we deduce that
272 the bulk of this solid residue was initially an ACC that actively rejected Mg^{2+} during exsolution.
273 Consistent with this assertion, XRD analysis of the residual solids from experiment E_{11}

identifies them as aragonite associated with the hydrated Mg-carbonate dypingite (Fig. S1). This assemblage directly reflects the bulk saturation state (SI_{Arag} = 2.41 and SI_{Hmag} = 5.01; Table S1), while the kinetic inhibition of dolomite persists despite its high thermodynamic potential ($SI_{Dol} \geq 5.54$). The result is consistent with solid-state transformation of the initial ACC, which segregated into distinct Ca and hydrated-Mg phases upon aging and dehydration at ambient temperature.

During the active synthesis stage (S_{ii}), Ca removal continued, reaching between 65–84% across all experiments. Following stabilization (S_{iii}), most conditions exceeded 95% removal, except for the functionalized, and electrochemically active experiment (E_{11}, ~75%), where ligand complexation and interfacial electrochemical dynamics rendered it unavailable for co-precipitation (Fig. 4B; Table 1).

3.3.3. Manganese removal: Redox-driven sequestration

Mn removal exhibited a distinct, redox-driven pattern compared to Mg. After 20 doses of the Mg-Ca reactant (S_{ii}), removal of Mn varied across experimental conditions, and showed the strongest kinetic response to electrochemical treatment. Accordingly, Mn removal ranged from 10.2 ± 7.2% to 61.4 ± 17.3%, with electrochemical sweeping without functionalization (E_{01}) yielding the highest scavenging efficiency, far exceeding both the only functionalized experiment (E_{10}) and the control (E_{00}). Remarkably, after the 24 h equilibration (S_{iii}), Mn depletion approached >99% in most conditions, indicating near-complete incorporation into the solid phases. The significant exception occurred in E_{11} (electrochemical + functionalized), where 25–38% of the total Mn remained in solution. This indicates that while the potential sweep drives oxidation-reduction, some of the carboxyl ligands in E_{11} can stabilize a significant fraction of the manganese available in the system (see Tordi et al., 2025), thus preventing the almost complete sequestration observed in non-functionalized controls (Fig. 4C; Table 1).

3.4 Mineralogical and textural characterization of precipitates

Neither electrochemical cycling nor functionalization alone produced dolomite-composition-like phases. Controls (E_{00}) yielded only minimal, sparse Mn-rich precipitates on the WE (Fig. 5A). Functionalization without electrochemistry (E_{10}) increased precipitate density, forming manganous Mg-Ca carbonate spheroids (Fig. 5B–C). TEM in various modes (Fig 5D-F) showed that the crystallites comprising these fabrics grow outward from central nucleation points, forming spherulitic structures with radially arranged crystallites.

Electrochemical cycling without functionalization (E01) yielded disperse aggregates resulting from the rapid coalescence of multiple nanocrystalline domains. In these experiments, a Mg-carbonate phase forming rosettes was observed (Fig. 6A). The delicate texture—likely a hydrous phase—was unstable under the ion beam and could not be recovered during FIB-lamella preparation (Fig. 6B). STEM-HAADF imaging reveals that the recovered aggregates exhibited significant internal porosity ("vuggy"), consistent with self-assembly during growth (Fig. 6C). Chemically, these aggregates display a magnesian-calcian rhodochrosite composition. It displays distinct zoning indicated by Z-contrast gradients portraying denser Mn-enriched domains transitioning into Ca-enriched inner domains, and with Mg homogenously distributed along the spheroids (Fig. 6C–E). SAED ring assignments generated a d_{104} spacing of ~2.84 Å, alongside d_{113} (2.39 Å) and d_{110} (2.16 Å) reflections (Fig. 6F).

Condition E_{11} yielded dense carbonate coatings consisting of 1–3 μm polycrystalline spheroidal aggregates (Fig. 7A–C). Internally, these aggregates are defined by the coalescence of smaller (200–600 nm) spheroids with Mn-enriched, thread-like cores and variably Mg-enriched cortices (Fig. 7C–D). TEM-EDS confirms preferential Mn partitioning in the cores, with oscillatory zoning likely induced by potential swapping (Fig. 7E). To resolve the potential for solid solution extending to the dolomite-kutnohorite series (*cf.* Peacor et al., 1987), we plotted these EDS data on a ternary Ca-Mg-Mn diagram (Fig. 7H). The data reveal a continuous

kinetic trajectory where metastable magnesian-calcian rhodochrosite, formed in the cores, transition into manganoan protodolomite cortices. Notably, these intermediate compositions plot directly within the thermodynamic miscibility gap defined by Peacor et al. (1987), indicating that rapid kinetic growth stabilized a continuous solid solution that reflects disequilibrium crystallization. In contrast, the E_{01} as magnesian- rhodochrosite products cluster distinctly at the magnesite- calcian rhodochrosite solvus (Fig. 7H); the E_{01} phase is presumably stable.

Structurally, HRTEM reveals that our two-phase manganoan carbonate spheroids posses a mosaic texture composed of nanodomains separated by broad, diffuse low-angle boundaries (Fig. 7F). FFT analysis (Fig. S3) confirms slight crystallographic misorientations (3–11°) between these regions. Diffraction rings in the SAED patterns (Fig. 7G) confirm that E_{11} yielded a polycrystalline, randomly oriented precipitate. The measured interplanar distances of the cores are consistent with disordered kutnahorite, while the cortices exhibit reflections consistent with a disordered dolomite with near-stoichiometric cation ratio (i.e., Ca : (Mg + Mn) = 1) as per d_{104} *ca*. 2.88 Å. Other reflections that can confidently assigned are d_{101} (4.029 Å), d_{110} (2.404 Å), d_{113} (2.191 Å), and d_{116} (1.786 Å). The characteristic *b*-type superstructure reflections (e.g., d_{015}, d_{021}, etc), which signify cation ordering, were unresolved.

3.5 EELS of the cortical precipitates

The results from EELS targeting the synthetic products from E_{11} are shown in Figure 8A-D. The carbon K-edge spectra are characterized by sharp pre-edge peaks at 290.4 eV and broader features at 300.9 eV, corresponding to the π* and σ* resonances of the C=O bond, respectively. These transitions combined with corresponding O *K*-edges at ~531 eV, uniquely identify the matrix as carbonate (Fig. 8A-B). The Ca $L_{3,2}$-edge (Fig. 8C) shows well-resolved spin-orbit splitting (L_3 at 349 eV), confirming the integration of Ca into a crystal lattice. Most significantly, the spectra capture characteristic Mn $L_{3,2}$-edge features in the 640 to 650 eV range

(Fig. 8D). Mn $L_{2,3}$ edge spectra ($N = 4$) from the core of a representative spheroid were analyzed using the deep-learning framework MnEdgeNet (Ji et al., 2023). The Supplementary Material (Fig. S4) contains the MnEdgeNet modelling results. The combined data exhibit L_3/L_2 white line intensity ratio ≈ 2.88 with an L_3 absorption maximum located at 639.5–640.0 eV. The applied MnPredictor decomposition was the 'noise-free' model, which prioritizes peak position fidelity and spectral shape. It returned to an average oxidation state (AOS) of +2.03, indicating ≥98.6% Mn(II) (Fig. 8D). This predominantly divalent state is physically confirmed by the deep spectral valley between the L_3 and L_2 edges (arrow in Fig. 8D), which reaches baseline intensity.

4. Discussion

We presented an electrochemical pathway that circumvents the kinetic barriers inhibiting the incorporation of the Mg^{2+} ion by leveraging the redox chemistry of Mn on a functionalized surface of graphite WEs. The enhanced Mn removal rates (61%) under potential cycling, compared to non-electrochemical controls, confirm that applied potential acts as the primary driver for precursory double-cation carbonate formation (i.e., disordered magnesian kutnahorite and manganoan protodolomite). This low-temperature synthesis results establish a mechanistic link between manganese redox cycling (Petrash et al, 2015), organic functionalization and ionic lattice distort (Han et al., 2024), the low-temperature nucleation of manganoan dolomite, and the increasingly recognized role of electron transfer mechanisms in marine sediments (Nielsen et al., 2010). Aqueous analysis confirms that a kinetic control is governed by the synergy between the metal cations and the carboxy ligand near the reactive (electroactive) surface. Cyclic voltammetry demonstrates that carboxyl functionalization modulates the electrochemical behavior of manganese, facilitating quasi-reversible Mn(II) ↔Mn(III) valence state transitions that are otherwise kinetically inhibited at the WE interface. Our central finding is the formation of compositionally zoned spheroids, which feature Ca-Mn-

373 enriched cores and Mg-enriched cortices. In the absence of carboxyl, the observation of vuggy
374 textures, characterized by irregular open voids within the aggregates suggests a rapid
375 coalescence mechanism. The discussion below expands on observations, their interpretations
376 and implications.

377 **4.1 The Mn-templating mechanism**

378 Morphological and nanostructural characterization reveals that low-temperature nucleation
379 proceeds via a heterogeneous, core-cortex pathway. In the solid-phase products of E_{11},
380 STEM-HAADF imaging, SAED, EDS mapping identify a Mn-rich core with minor Mg.
381 These serve as templates for the subsequent growth of a magnesium-enriched cortciesx—a
382 phase separation significantly promoted by carboxyl functionalization. In control experiments
383 lacking carboxyl groups, kutnahorite crystallites formed by a rapid coalescence mechanism
384 where individual nucleation centers merged to form spheroids, trapping fluid pockets during
385 growth, but lacking the marked phase transition observed in the functionalized system. The
386 E_{11} spheroidal cores are seen as analogous to "pseudo-kutnahorite" (Mucci, 1988), while the
387 EDS and SAED features of the cortices are consistent with a manganoan (proto)dolomite
388 precursor.

389 However, regarding SAED, it is worth noticing that the apparent absence of ordering
390 reflections may be a methodological artifact rather than intrinsic disorder. Relative thickness
391 mapping ($t(\lambda)^{-1}$) derived from the low-loss EELS spectrum reveals that the dolomitic cortices
392 correspond to the thinner regions of the lamellae yet these exhibit local $t(\lambda)^{-1}$ values ranging
393 from 0.86 to 0.88 (Fig. S5). In this regime, approximately 59-64% of the incident electrons
394 undergo inelastic scattering (Egerton, 2011). This substantial background contribution,
395 combined with the polycrystalline nature of our synthetic products, likely lowers the signal-
396 to-noise ratio sufficiently to obscure weak superlattice reflections possibly associated with
397 incipient cation ordering. Consequently, while the current SAED data are consistent with a

disordered precursor, the sample thickness was not optimal for definitively resolving any faint b-type reflections characteristic of substantial Ca occupancy in the B site. Attenuation of *b*-type reflections may also be from manganese occupying a substantial portion of the magnesium sites within this disordered lattice structure (Goldschmidt and Graf, 1960).

Although kutnahorite (the isostructural analogue to dolomite) is metastable at near-surface temperatures (Peacor et al., 1987; Mucci, 1991, 2004; Böttcher and Dietzel, 2010), our results show that formation of this metastable phase is kinetically favoured over dolomite under functionalized conditions. While thermodynamics alone dictates that dolomite is the more stable phase ($\Delta G^{o}f_{dol} < \Delta G^{o}f_{kutn}$; Rosenberg and Foit, 1979), kinetic factors—specifically those underlying the empirical Ostwald step rule, influence reaction pathway. Despite the bulk electrolyte being undersaturated with respect to kutnahorite (SI = -2.57; Table S1), the out-of-equilibrium experiments implemented here indicate that this precursor presents a significantly lower activation energy barrier to nucleation than oversaturated dolomite) (SI =5.54) . This advantage is probably rooted in coordination chemistry as Mn^{2+} has a lower magnitude of dehydration enthalpy compared to Mg^{2+} (-1851 *vs*. -1926 kJ mol^{-1}; Marcus, 1987), and its water exchange rate is nearly two orders of magnitude faster (2.1 10^{7} s^{-1} *vs*. 6.7 10^{5} s^{-1}; Helm & Merbach, 2005). This allows Mn^{2+} ions to desolvate and occupy the carbonate lattice rapidly, effectively bypassing the barrier that stalls Mg incorporation.

Other factors may also be at play. Pimentel et al. (2022) proposed that the high lattice strain inherent to dolomite (determined by its cationic mismatch ratio, $R_{Ca}/R_{Mg} \sim 1.38$) may contribute substantially to the energetic barrier inhibiting its formation at low temperature. In contrast, within the octahedral geometry, Mn^{2+} possesses an effective ionic radius ~15% larger than that of Mg^{2+} (0.83 Å *vs*. 0.72 Å; Shannon, 1976). This yields a significantly lower mismatch ratio for kutnahorite ($R_{Ca}/R_{Mn} \sim 1.20$) and places the latter phase within a (meta)stability window where lattice strain is sufficiently low to avoid the kinetic penalties

423 that prevent dolomite nucleation/growth. However, lattice-ordering in multicomponent
424 phases is governed by factors beyond simple cation radii (Jakob et al., 2025). In our system,
425 cation-partitioning can also be critical. Mucci (1988) and Böttcher (1998) demonstrated that
426 the Mg distribution coefficient (D_{Mg}) is notably higher in Mn-bearing environments. As the
427 [Mg]/([Mn]+[Ca] ratio progressively rises during precipitation, D_{Mg} increases, facilitating the
428 incorporation of Mg^{2+} into the Mn-expanded lattice of the kutnahoritic precursor. Being
429 manganoan, this phase—exhibiting a small lattice mismatch (<1.5%; a_{Kut} = 4.8732(8) Å, a_{Dol}
430 = 4.8012(1) Å), has some degree of structural distortion (Rosenberg and Foit, 1979).

431 HRTEM imaging reveals a mosaic nanostructure interpreted as local heterogeneities
432 in stoichiometry and cation ordering, separated by broad and diffused low-angle boundaries
433 (Fig. 7G). In double-cation carbonates, such variations force the coexistence of regions with
434 disparate unit cell parameters (Fang and Xu, 2019). The misorientations act as strain-
435 minimization structures and formed as the crystal progresses towards near-Mg-Ca
436 stoichiometry and thermodynamic equilibrium (Van Tendeloo et al., 1985). Within the (122)
437 domain, lattice non-linearity—manifested as bending and dislocations—indicates internal
438 compositional modulation, serving as the direct reciprocal-space signature of the lattice
439 relaxation required to relieve the multi-cation driven strain. The mechanism may also
440 circumvent the "step-pinning" barrier (Higgins and Hu, 2005) by stabilizing the strained
441 surface, thereby preventing the rapid monolayer dissolution inherent to slow Mg-dehydration.

442 **4.2 A synergy of carboxylates and redox potential oscillations**

443 The nucleation mechanism is governed by a strict synergy between organic functionalization
444 and the applied electrochemical potential sweep. In our view, this mimics the mechanisms
445 active at the reactive surface of sedimentary Mn-bearing phases that can be trapped within
446 microbial mats in modern chemically stratified dolomite-precipitating systems (e.g., Petrash
447 et al., 2015). The alginate hydrogel acts not merely as a passive cation-binding medium, but

as an active structural agent that alters crystallization kinetics, driving the distinct morphological and mineralogical outcomes (Braissant et al. 2003; Mercedes-Martín et al. 2016).

4.2.1. Morphological divergence and chemical zoning

The interplay between the polymer matrix and the electric field dictates the growth habit. In the passive functionalized condition (E_{10}), precipitation follows a radial, isotropic pathway. Here, despite the presence of the biopolymer, nucleation propagates randomly from the initial seed. As described by Gránásy et al. (2005), such 'disorder disrupts the crystalline anisotropy early in the growth process', leading to rapid spherical symmetrization.

In contrast, the synergy of carboxyl functionalization and electrochemistry in E_{11} shifts the system toward the Category 2 growth mode of Gránásy et al. (2005). In this experiment, the polarized alginate chains may establish a directional electric field along the hydrogel, inducing an initial fibrillar habit by stabilizing metal ions. The cyclic redox changes modify the free-energy landscape (De Yoreo et al., 2015), creating conditions where kinetic barriers favour low-angle, non-crystallographic branching over coherent lattice extension. Consequently, the initial fibers splay into crystal sheaves rather than coalescing isotropically, forming the 'eye-like' spherulitic aggregates. High-resolution imaging confirms that a dense, nanogranular fabric—consistent with non-classical particle attachment—serves as the initial nucleation anchor for these diverging sheaves (Fig. 5).

The distinct core-shell zoning observed in E11 reflects transport-controlled partitioning in a diffusion-limited regime (Prieto et al., 1997). While data plotting within the thermodynamic miscibility gap (Fig. 7H) must be interpreted with caution due to the potential for analytical averaging of sub-micron phases, the coherent, continuous trajectory from Mn-rich cores to Mg-rich rims suggests a primary geochemical signal. This trend implies rapid,

metastable precipitation driven by progressive pore-fluid Mn depletion, where kinetic growth rates outpaced thermodynamic re-equilibration, forcing the precipitating carbonate solid solution to continuously bridge the miscibility gap.

4.2.2. The electrochemical "engine": ligand tethering and cation pumping

At the molecular level, specific orbital interactions drive this engine. According to frontier molecular orbital theory, the reoxidation of aqueous Mn(II) requires the displacement of water by anionic ligands to proceed via an inner-sphere mechanism (Luther, 2005). The alginate carboxyl groups fulfill this requirement, facilitating electron transfer to the electroactive Mn-reactant (Fig. 9A). As the local activity of Mn is progressively depleted, these same ligands transition to binding the increasingly abundant Mg^{2+} ions (Fig. 9B). This transition relies on the pre-existing Mn-rich substrate; rooted in ionic radius compatibility and enhanced Mg-partitioning (Mucci, 1988; Böttcher, 1998), the initial kutnohoritic core acts as a lattice bridge, lowering the interfacial energy barrier for Mg-carbonate epitaxy.

Critically, the system utilizes proton-coupled redox cycling to actively mobilize reactants from the surficial hydrogel. This mechanism is fueled by localized interfacial acidification arising from two synergistic sources: (i) carbonate precipitation, and (ii) the stoichiometric proton release coupled to the anodic oxidation of Mn(II) (Fig. 3B). Estimates using a steady-state Nernst approximation suggest this anodic flux induces a local acidification (ΔpH ~ -0.5 to -1.2 units) within the diffusion boundary layer at the WE surface (see Supplementary Note S1 in the Supplement). This transiently protonates the carboxyl ligands (pKa ~4), triggering the "depinning" of cross-linked cations—Mg^{2+}, Mn^{2+}, and Ca^{2+}; for co-incorporation into growing cortices (Fig. 9B). Transient accumulation of H^+ near the reactive (electroactive) surface may create oscillating saturation states required to feed non-classical cluster coalescence (De Yoreo et al., 2015) and generate oscillatory cortical zoning (e.g., Katsikopoulos et al., 2009) that we ascribe to disequilibrium processes.

Finally, carboxyl functionalization alters the thermodynamic fate of the intermediate Mn species. As delineated by the Eh-pH stability fields (Fig. S6), the applied potential sweep (-0.1 to +0.4 V) and pH_{surf} variability (±1.2 units) initiates at the solubility 'tipping point' of hausmannite (Mn_3O_4) and manganite (MnOOH) (Stumm & Morgan, 1996, Faust & Ally, 1998). In a purely inorganic system, this trajectory triggers rapid Mn(III) disproportionation and irreversible reactant loss (Luther, 2005). However, as evidenced by cyclic voltammetry, the ligand-free interface (E_{01}) is kinetically inhibited, showing negligible faradaic activity. Substantial Mn removal observed in this experiment (61%, Table 1) thus act as a control for readily occurring, non-mediated carbonate precipitation consuming reactant cations. In stark contrast, functionalization in E_{11} enables the quasi-reversible (electrochemical) regeneration of Mn(III) in the system (Fig. 3), isolating a fraction of it from precipitation. This paradoxically results in lower net Mn removal (29%, Table 1), confirming that the carboxyl ligand field induces kinetic stabilization of Mn(III) in the hydrogel and progressive Mn(II) incorporation in carbonate. The ligands allow the electrode to reductively cycle Mn(III) and sustain the redox pump (Fig. 9A-B), avoiding the irreversible loss observed in E_{01}. Thus, the organic matrix transforms the system from a passive chemical sink into an active electrochemical engine (Eq. 3):

$$[R\text{-}COO\text{-}Mn^{III}(OH)] + e^- + H^+ \rightarrow [R\text{-}COO\text{-}Mn^{II}] + H_2O \quad (3)$$

4.3. Broader geo(bio)logical implications

4.3.1. Resolving the synsedimentary deep time dolomite paradox

In this section we interpret Mn-rich bands typically seen in dolomite crystals as a persistent chemo-textural fingerprint of Mn-catalysis. Lithostratigraphic and sedimentological metadata on the dolostone deposits considered in this section are listed in Supplementary Note S2. The interpretation presented here considers the punctuated massive co-occurrence of Precambrian

(Shang, 2023) and Phanerozoic dolostones (Li et al., 2022) in light of sedimentary manganese depositional pulses (Spinks et al., 2022, Robbins et al., 2023; Fig. 10A).

The "Mn pump" conspicuously operated during the Paleoproterozoic (~2.3–2.05 Ga), linking kutnohorite formation with dolomite (e.g., Nyame, 2008; Préat et al., 2011; Nzamba et al., 2026). By Mesoproterozoic dolomite exhibit a relative abundance peak. Relevant Calymmian-Ectasian (1.6-1.2 Ga) dolomite accumulations occurred in the McArthur Basin, which hosts massive fabric-retentive members with well-preserved early eukaryote cells and their Mn-mineralized sheaths (Muir 1976, 1983)—supporting Mn-catalysis as a preservation agent in ancient dolostone deposits (Bontognali, 2019). By this Period, newly quantified sedimentary Mn ores challenge the concept of a complete mechanistic hiatus in Mn deposition (Spinks et al., 2022; Xu et al., 2025), which would otherwise invalidate the coupling proposed here. The mechanisms require redox-stratified water columns episodically fed by Mn(II) of hydrothermal origin (Johnson et al., 2016; Robbins et al., 2023) — conditions that were likely disrupted by Mesoproterozoic tectonic stability and expanding euxinia (Poulton et al., 2010; Planavsky et al., 2014), leading to important local minima (Fig. 10A).

The dynamic re-emerged in the Neoproterozoic. High terrigenous Mn fluxes and benthic microbial activity during the Tonian (Liang et al., 2025) and Cryogenian–Ediacaran interglacials (Fig.10A–B) fully re-established conditions for syndiagenetic, fabric retentive dolomite formation (Hood et al., 2011; Stacey et al., 2023). These factors, amplified by weathering fluxes and widespread coastal (i.e., microbial) paleoproductivity (Le Hir et al., 2008; Cai et al., 2023; Fang and Xu, 2022), may explain the distinctive chemo-textural features of globally distributed Ediacaran shallow-marine carbonate deposits (Hood et al., 2011, 2012; Wood et al., 2018; Chang et al., 2020; Stacey et al., 2023, ; Wilcots et al., 2025; Ren, 2025).

546 *4.3.2. Phanerozoic decoupling and restriction to continental basins*

547 As the Earth system transitioned toward a fully oxygenated state (Fig. 10B), Phanerozoic
548 deep-ocean ventilation generally disrupted the shallow-water 'Mn-pump' (Davies & Morgan,
549 1989; Chen et al., 2023; Spinks et al., 2022; Robbins et al., 2023) . Consequently, the global
550 correlation between dolomite and Mn-deposits faded (Fig. 10A) as Precambrian Mn-
551 carbonates progressively gave way to oxidized phases (Roy, 2006; Maynard, 2010; Johnson
552 et al., 2016). However, this long-term decoupling was punctuated during Paleozoic and
553 Mesozoic ocean anoxia (Zhang et al., 2020; Yan et al., 2022). In these intervals, transient
554 redox stratification (Fig. 10B; Li et al., 2021) likely reactivated the oxidative Mn-cycling
555 required for episodic Mn(II)-carbonate development (Robbins et al. 2023). Future systematic
556 analysis of redox proxies in dolostone (e.g., Zhang et al., 2020) may further substantiate this
557 oceanographic-stratigraphic coupling. Finally, by the Cenozoic, Mn-oxides became
558 dominant, reflecting high global oxidation potentials; yet the templating mechanism persisted
559 in non-marine 'refuges' mimicking Precambrian Mn–N redox dynamics (Petrash et al., 2025).
560 Our model provides a mechanistic basis for observations in the Eger Rift paleolake, Lake
561 Van (McCormack et al., 2018; McCormack et al., 2023), and post-Pliocene sabkha deposits
562 (Chafetz et al., 1999; Di Loreto et al., 2021).

563 **5. Conclusions**

564 We demonstrate that coupling manganese redox cycling with carboxyl functionalization
565 unlocks a kinetically facile pathway for the low-temperature formation of dolomite-group
566 minerals. Our results show that electrochemical modulation accelerates Mn sequestration by
567 over 60% compared to passive controls, generating a disordered (pseudo-)kutnahorite
568 template that circumvents the high activation energy of Mg^{2+} dehydration. This templating
569 mechanism enables the epitaxial growth of disordered dolomite in <24 h—a process that
570 otherwise requires longer synthesis. By proposing and empirically testing a specific non-

equilibrium mechanism this work advances a predictive paragenetic framework that can be applied to evaluate the stratigraphic abundance of ancient syndiagenetic dolomite. In this regard, we demonstrated how this mechanism may be instrumental in resolving the deep-time paradox of widespread Neoproterozoic and Paleoproterozoic fabric-retentive dolomite, as well as explaining the decline and eventual (punctuated) dolostone abundance throughout the Phanerozoic rock record.

6. Future work

Moving forward, differentiating this electrochemical signal from burial diagenesis requires robust petrography, reliable geochemical fingerprinting and refined nanoscale characterization. A significant technical hurdle remains the preparation of optimal FIB lamellae from these inherently friable, polycrystalline aggregates. While single-crystal diffraction would theoretically provide the definitive resolution for cation ordering, the pervasive polycrystalline nature of the spheroid precluded the isolation of discrete, defect-free domains large enough for standard tilt-series analysis. Consequently, future work must focus on optimizing ion polishing protocols—potentially identifying rare single-crystal domains—to achieve the ideal electron transparency ($(\lambda)^{-1} < 0.5$) required to resolve whether faint superlattice reflections are present. Simultaneously, future research should prioritize constraining specific isotopic fractionation factors (e.g., $\delta^{26}Mg$, $\delta^{13}C$-$\delta^{18}O$, Δ_{47}-Δ_{48} REE systematics) associated with this pathway, and with extended synthesis until electrode passivation. To achieve this, experimental redesign can transition from closed-system batch reactors to continuous-flow 'chemostat' setups under controlled pCO_2 atmospheres. Reengineering of this setup may allocate future work to systematically target the saturation states characteristic of ancient 'greenhouse' intervals. By maintaining constant reactant activities (e.g., via external DIC buffering), reengineered pH-stat electrochemical precipitation apparatus must mitigate cation depletion artifacts imposed by instantaneous

596 homogeneous precipitation of ACC, enabling the precise determination of equilibrium
597 distribution coefficients (K_D) that would otherwise remain elusive in drift-dominated low
598 temperature dolomite precipitation environments.

599 **Acknowledgement**

600 This is a contribution to the Strategic Research Plan of The Czech Geological Survey
601 (DKRVO/CGS 2023-2027, 311670). This study received funding from the EU Horizon
602 Europe research and innovation programme under grant agreement No 101131765
603 (EXCITE2) for Transnational Access to Advanced Microscopy facilities at Utrecht
604 University.

605 **References**

606 Al Disi, Z.A., Zouari, N., Attia, E., Al-Asali, M., Al-Kuwari, H.A.S., Sadooni, F., Dittrich,
607 M., Bontognali, T.R., 2021. Systematic laboratory approach to produce Mg-rich
608 carbonates at low temperature. RSC Advances 11, 37029–37039.

609 Al Disi, Z. A., Zouari, N., & Bontognali, T. R. (2024). Dissolved silicon as a beneficial factor
610 for biomineralization of disordered dolomite by a halophilic cyanobacterium. *Chemical*
611 *Geology*, 670, 122435.

612 Aljinović, D., Richoz, S., Smirčić, D., Chen, Y., Nestell, G., Jazvac, I., & Petrash, D. A.
613 (2025). Features and dolomitizing mechanisms in inner platform facies across the
614 Permian–Triassic boundary (External Dinarides, Croatia). *Sedimentology*, *72*(3), 822–
615 843. doi: 10.1111/sed.13257

616 Baniak, G. M., Amskold, L., Konhauser, K. O., Machel, H. G., & Gingras, M. K. (2014).
617 Sabkha dolomite formation within burrowed stromatolites of the Devonian Grosmont
618 Formation. *Sedimentology*, 61(5), 1254-1272.

619 Berner, R. A. (1991). A model for atmospheric CO_2 over Phanerozoic time. *American*
620 *Journal of Science*, 291(4), 339-376.

621 Bischoff, J. L. (1968). Kinetics of calcite nucleation: Magnesium ion inhibition and ionic
622 strength catalysis. *Journal of Geophysical Research*, *73*(10), 3315–3322.

623 Braissant, O., Cailleau, G., Dupraz, C. and Verrecchia, A.P.J. (2003) Bacterially induced
624 mineralization of calcium carbonate in terrestrial environments: the role of
625 exopolysaccharides and amino acids. J. Sed. Res., 73, 485–490.

626 Bontognali, T.R.R., McKenzie, J.A., Warthmann, R.J., Vasconcelos, C., 2014. Microbially
627 influenced formation of Mg-calcite and Ca-dolomite in the presence of exopolymeric
628 substances produced by sulphate-reducing bacteria. Terra Nova 26, 72–77.
629 https://doi.org/10.1111/ter.12072

630 Bontognali, T.R.R., Vasconcelos, C., Warthmann, R.J., Bernasconi, S.M., Dupraz, C.,
631 Strohmenger, C.J., McKenzie, J.A., 2010. Dolomite formation within microbial mats in
632 the coastal sabkha of Abu Dhabi (United Arab Emirates). Sedimentology 57, 824–844.

633 Bontognali, T.R.R (2019). Anoxygenic phototrophs and the forgotten art of making dolomite.
634 *Geology,* 47 (6), 591–592.

635 Böttcher, M.E. (1998) Manganese(II) partitioning during experimental precipitation of
636 rhodochrosite-calcite solid-solutions from aqueous solutions. *Marine Chemistry,* 62, 287-
637 297.

638 Böttcher M.E. & Dietzel M. (2010) Metal-ion partitioning during low-temperature
639 precipitation and dissolution of anhydrous carbonates and sulfates. EMU Notes in
640 Mineralogy 10, 139-187.

641 Cai, Y., Wallace, M. W., Hua, H., & Hood, A. (2023). Interlinked marine cycles of methane,
642 manganese, and sulfate in the post-Marinoan Doushantuo cap dolostone. *Geochimica et*
643 *Cosmochimica Acta*, 346, 160-179.

644 Chafetz, H. S., Imerito-Tetzlaff, A. A., & Zhang, J. (1999). Stable-isotope and elemental
645 trends in Pleistocene sabkha dolomites: Descending meteoric water *vs*. sulfate reduction.
646 *Journal of Sedimentary Research*, *69*(1), 256–266.

647 Chen, G., Cheng, Q., Lyons, T.W., Shen, J., Agterberg, F., Huang, N., Zhao, M. (2022).
648 Reconstructing Earth's atmospheric oxygenation history using machine learning. *Nat.*
649 *Commun.* 13, 586.

650 Chen, F., Wang, Q., Pufahl, P. K., Matheson, E. J., Xian, H., Nan, J., Ma, H., & Deng, J.
651 (2023). Carbonate-hosted manganese deposits and ocean anoxia. *Earth and Planetary*
652 *Science Letters*, 622, 118385.

653 Davies, S.H.R. & Morgan, J.J., (1989). Manganese(II) oxidation kinetics on metal oxide
654 surfaces. *Journal of Colloid and Interface Science* 129, 63–77.

655 Daye, M. E., Klepac-Ceraj, V., & Bosak, T. (2019). Anoxygenic phototrophs and the
656 forgotten art of making dolomite. *Geology*, 47(6), 509-512.

657 De Yoreo, J.J., Gilbert, P.U.P.A., Sommerdijk, N.A.J.M., Penn, R.L., Whitelam, S., Joester,
658 D., Zhang, H., Rimer, J.D., Navrotsky, A., Banfield, J.F., Wallace, A.F., Michel, F.M.,
659 Meldrum, F.C., Cölfen, H. and Dove, P. (2015) Crystallization by particle attachment in
660 synthetic, biogenic, and geologic environments. *Science*, 349, 1–9.

661 Di Loreto, Z.A., Garg, S., Bontognali, T.R., & Dittrich, M., 2021. Modern dolomite
662 formation caused by seasonal cycling of oxygenic phototrophs and anoxygenic
663 phototrophs in a hypersaline sabkha. *Scientific Reports* 11, 4170.

664 Egerton, R. F. (2011_. Electron Energy-Loss Spectroscopy in the Electron Microscope, 3rd
665 ed. Springer, New York.

666 Fang, Y., & Xu, H. (2022). Dissolved silica-catalyzed disordered dolomite precipitation.
667 *American Mineralogist*, 107(5), 882-891.

668 Fang, Y., & Xu, H. (2022). Coupled dolomite and silica precipitation from continental
669 weathering during deglaciation of the Marinoan Snowball Earth. *Precambrian Research*
670 380, 106824.

671 Faust, S. D., & Aly, O. M. (1998). *Chemistry of water treatment*. CRC Press.

672 Frondel, C., & Bauer, L. H. (1955). Kutnahorite: a manganese dolomite, $CaMn(CO_3)_2$.
673 *American Mineralogist*, 40, 748-760.

674 Given, R.K., Wilkinson, B.H. (1987). Dolomite abundance and stratigraphic age, constraints
675 on rates and mechanisms of dolostone formation. *J. Sediment. Petrol.* 57, 1068–1078.

676 Graf, D. L., & Goldsmith, J. R. (1956). Some hydrothermal syntheses of dolomite and
677 protodolomite. *The Journal of Geology*, 64(2), 173-186.

678 Gránásy, L., Pusztai, T., Tegze, G., Warren, J. A., & Douglas, J. F. (2005). Growth and form
679 of spherulites. *Physical Review E*, 72(1), 011605.

680 Han, Z., Zhang, F., Farfan, G. A., & Xu, H. (2024). Dissolved Mn2+ promotes microbially-
681 catalyzed protodolomite precipitation in brackish oxidized water. *Chemical Geology*, 650,
682 121986.

683 Helm, L., & Merbach, A. E. (2005). Inorganic and bioinorganic solvent exchange
684 mechanisms. *Chemical Reviews*, 105(6), 1923–1959.

685 Higgins, S. R., & Hu, X. (2005). Self-limiting growth on dolomite (104) surfaces.
686 *Geochimica et Cosmochimica Acta*, 69(8), 2085-2094.

687 Holland, H. D., & Zimmerman, H. (2000). The dolomite problem revisited. *International*
688 *Geology Review*, 42(6), 481-490.

689 Hood, A. v. S., Wallace, M. W., & Drysdale, R. N. (2011). Neoproterozoic marine dolomite
690 hardgrounds and their relationship to cap dolomites. *Precambrian Research*, 188(1-4),
691 118-134.

692 Hood, A. v. S., & Wallace, M. W. (2012). Synsedimentary recrystallization of
693 Neoproterozoic reef carbonates. *Sedimentary Geology*, 255, 56-71.

694 Jakob, K. S., Walsh, A., Reuter, K., & Margraf, J. T. (2025). Learning Crystallographic
695 Disorder: Bridging Prediction and Experiment in Materials Discovery. *Advanced*
696 *Materials*, e14226.

697 Ji, Z., Hu, M., & Xin, H. L. (2023). Mn-EdgeNet for accurate decomposition of mixed
698 oxidation states for Mn XAS and EELS L2,3 edges without reference and calibration.
699 *Scientific Reports*, 13, 14132.

700 Ji, D., Park, J. M., Oh, M. S., Nguyen, T. L., Shin, H., Kim, S. L., Kim, D., & Kim, J. (2022).
701 Superstrong, superstiff, and conductive alginate hydrogels. *Nature Communications*, 13,
702 3019.

703 Johnson, J. E., Webb, S. M., Ma, C., & Fischer, W. W. (2016). Manganese mineralogy and
704 diagenesis in the sedimentary rock record. *Geochimica et Cosmochimica Acta*, *173*, 210–
705 231.

706 Jørgensen, B. B., Revsbech, N. P., Blackburn, T. H., & Cohen, Y. (1979). Diurnal Cycle of
707 Oxygen and Sulfide Microgradients and Microbial Photosynthesis in a Cyanobacterial
708 Mat Sediment. *Applied and Environmental Microbiology*, *38*(1), 46–58.

709 Kaczmarek, S. E., & Sibley, D. F. (2014). On the evolution of dolomite stoichiometry and
710 cation order during high-temperature synthesis experiments: An alternative model for the
711 geochemical evolution of natural dolomites. *Sedimentary Geology*, 301, 32-43.

712 Kaczmarek, S. E., & Thornton, B. P. (2017). The nature of the dolomite (104) peak, and its
713 implication for interpreting the degree of cation order in high-temperature synthesis
714 experiments. *Chemical Geology*, 470, 148-161.

715 Katsikopoulos, D., Fernández-González, Á., & Prieto, M. (2009). Crystallization behaviour
716 of the (Mn,Ca)CO3 solid solution in silica gel: nucleation, growth and zoning
717 phenomena. *Mineralogical Magazine*, 73(2), 269–284.

718 Katz, A., & Matthews, A. (1977). The dolomitization of $CaCO_3$: An experimental study at
719 252–295 °C. *Geochimica et Cosmochimica Acta*, 41(2), 297–308.

720 Kell-Duivestein, I. J., Baldermann, A., Mavromatis, V., & Dietzel, M. (2019). Controls of
721 temperature, alkalinity and calcium carbonate reactant on the evolution of dolomite and
722 magnesite stoichiometry and dolomite cation ordering degree - An experimental
723 approach. *Chemical Geology*, 529, 119292.

724 Li, M., Song, H., Algeo, T. J., Wignall, P. B., Dai, X., & Woods, A. D. (2018). A
725 dolomitization event at the oceanic chemocline during the Permian-Triassic transition.
726 *Geology*, *46*(12), 1043–1046.

727 Li, M., Wignall, P. B., Dai, X., Hu, M., & Song, H. (2021). Phanerozoic variation in dolomite
728 abundance linked to oceanic anoxia. *Geology*, *49*(6), 698–702.

729 Lippmann, F. (1973). *Sedimentary carbonate minerals*. Springer-Verlag, Berlin, Heidelberg.

730 Luther, G. W. (2005). Thermodynamics and kinetics of manganese (II) oxidation and Mn
731 (IV) reduction in the environment: Two one-electron transfer steps versus a single two-
732 electron step. *Geomicrobiology Journal*, 22(3-4), 195-203.

733 Marcus, Y. (1987). Thermodynamics of ion hydration and its interpretation in terms of a
734 common model. Pure and Applied Chemistry 59, 1093-1101.

735 Maguire, M. E., & Cowan, J. A. (2002). Magnesium chemistry and biochemistry. *BioMetals*,
736 *15*, 203–210.

737 Maynard, B. (2010). The Chemistry of Manganese Ores through Time: A Signal of
738 Increasing Diversity of Earth-Surface Environments. Econ. Geol. 2, 105, 535–552

739 McCormack, J., Bontognali, T.R.R., Immenhauser, A., Kwiecien, O., 2018. Controls on
740 Cyclic Formation of Quaternary Early Diagenetic Dolomite. Geophysical Research
741 Letters 45, 3625–3634.

742 McCormack, J., Baldermann, A., Bontognali, T.R.R., Wolf, A., Kwiecien, O., 2024.
743 Hydrochemical mixing-zones trigger dolomite formation in an alkaline lake.
744 Sedimentology 71, 871–886.

745 McKenzie, J. A. (1991). The dolomite problem; an outstanding controversy. *Controversies in*
746 *modern geology: Evolution of geological theories in sedimentology, earth history and*
747 *tectonics*, 37-54.

748 Meister, P.H., Frisia, S., Dódony, I., Pekker, P., Molnár, Z., Neuhuber, S., Gier, S., Kovács,
749 I., Demény, A., & Pósfai, M. (2023). Nanoscale Pathway of Modern Dolomite Formation
750 in a Shallow, Alkaline Lake. Crystal Growth & Design, 23(5), 3202–3212.

751 Meister, P.H. (2025) Spherulitic mineral growth: auto-deformation, growth front nucleation
752 or semi-oriented attachment? In: *Nucleation and Growth of Sedimentary Minerals* (Eds
753 P.H. Meister, C. Fischer and N. Preto), *Int. Assoc. Sedimentol. Spec. Publ.,* 50, 171–189.

754 Meng, R., Han, Z., Gao, X., Zhao, Y., Han, C., Han, Y., Yang, R., Li, S., Liu, F., Tucker, M.
755 E., & Yan, H. (2024). Dissolved ammonia catalyzes proto-dolomite precipitation at Earth
756 surface temperature. *Earth and Planetary Science Letters*, 646, 119012.

Mercedes-Martín, R., Rogerson, M.R., Brasier, A.T., Vonhof, H.B., Prior, T.J., Fellows, S.M. & Pedley, H.M. (2016). Growing spherulitic calcite grains in saline, hyperalkaline lakes: experimental evaluation of the effects of Mg-clays and organic acids. *Sed. Geol.*, 335, 93–102.

Mucci, A. (1988). Manganese uptake during calcite precipitation from seawater: Conditions leading to the formation of a pseudo-kutnahorite. *Geochimica et Cosmochimica Acta*, *52*(7), 1859–1868.

Mucci, A. (1991). The solubility and free energy of formation of natural kutnahorite *Canadian Mineralogist,* 29, l13-12.

Mucci, A. (2004) The behavior of mixed Ca–Mn Carbonates in water and seawater: Controls of manganese concentrations in marine porewaters. *Aquatic Geochemistry*, 10, 139-169.

Muir, M. D. (1976). Proterozoic microfossils from the Amelia Dolomite, McMrthur Basin, Northern Territory. *Alcheringa*, 1(2), 143–158.

Muir, M. D. (1983). Proterozoic microfossils from the Mara Dolomite Member, Emmerugga Dolomite, McArthur Group, from the Northern Territory, Australia. *Botanical Journal of the Linnean Society*, 86(1–2), 1–18.

Nielsen, L. P., Risgaard-Petersen, N., Fossing, H., Christensen, P. B., & Sayama, M. (2010). Electric currents couple spatially separated biogeochemical processes in marine sediment. *Nature*, 463(7284), 1071-1074.

Nyame, F. K. (2008). Petrography and geochemistry of intraclastic manganese-carbonates from the ~2.2 Ga Nsuta deposit of Ghana: Significance for manganese sedimentation in the Palaeoproterozoic of West Africa. *Journal of African Earth Sciences*, *50*(2–4), 133–147.

780 Nzamba, K. X., Juhkama, H. R., Moussavou, M., Mayika, K. B., Kreitsmann, T., Lepland,
781 A., Prave, A. R., & Kirsimäe, K. (2026). Carbonate diagenesis and Mn-carbonate
782 formation in the Paleoproterozoic Francevillian succession (Lastoursville sub-basin) of
783 Gabon. *Journal of African Earth Sciences*, *235*, 105971.

784 Oomori, T., & Kitano, Y. (1987). Synthesis of protodolomite from seawater containing
785 dioxane. *Geochemical Journal*, 21(2), 59-65.

786 Peacor, D. R., Essene, E. J., & Gaines, A. M. (1987). Petrologic and crystal-chemical
787 implications of cation order-disorder in kutnahorite [CaMn(CO3)2]. *American*
788 *Mineralogist*, 72(3-4), 319-328.

789 Petrash, D. A., Roeser, P., Kříbek, B., Staudigel, P. T., Bernecker, M., Jačková, I., Čejková,
790 B., Kochergina, Y. V. E., Koubová, M., Křížová, Š., Knésl, I., Laufek, F., Böttcher, M.
791 E., Della Porta, G., & Fiebig, J. (2025). Drivers of episodic carbonate cementation during
792 the Miocene Climatic Optimum in a paleolake of the Eger Rift (Czech Republic).
793 *Geochimica et Cosmochimica Acta*, 407, 47–66.

794 Petrash, D. A., Lalonde, S. V., González-Guayaquil, A., Konhauser, K. O., & Méndez-
795 Vicente, A. (2015). Can Mn–S redox cycling drive sedimentary dolomite formation? A
796 hypothesis. *Geology*.

797 Petrash, D. A., Bialik, O. M., Bontognali, T. R., Vasconcelos, C., Roberts, J. A., McKenzie,
798 J. A., & Konhauser, K. O. (2017). Microbially catalyzed dolomite formation: From near-
799 surface to burial. *Earth-Science Reviews*, 171, 558-582.

800 Petrash, D. A., Lalonde, S. V., Raudsepp, M., & Konhauser K. O. (2011). Assessing the
801 Importance of Organic Matrix Materials in Biofilm Chemical Reactivity: Insights from
802 Proton and Cadmium Adsorption onto the Commercially Available Biopolymer Alginate.
803 Geomicrobiology Journal, 28 (3), 266-273.

804 Pimentel, C., Pina, C. M., & Sainz-Díaz, C. I. (2022). New Insights into Dolomite and
805 Dolomite-Analogue Structures from First Principles Calculations. *ACS Earth and Space*
806 *Chemistry*, 6(10), 2360-2367.

807 Pina, C. M., Pimentel, C., & Crespo, A. (2022). The Dolomite Problem: A Matter of Time.
808 *ACS Earth and Space Chemistry*, 6, 1468–1471.

809 Planavsky, N. J., Reinhard, C. T., Wang, X., Thomson, D., McGoldrick, P., Rainbird, R. H.,
810 Johnson, T., Fischer, W. W., & Lyons, T. W. (2014). Low mid-proterozoic atmospheric
811 oxygen levels and the delayed rise of animals. *Science*, *346*(6209), 635–638.

812 Polgári, M.; Bajnóczi, B.; Kis, Kovács V.; Götze, J.; Dobosi, G.; Tóth, M.; & Vigh, T. .
813 (2007). Mineralogical and cathodoluminescence characteristics of Ca-rich kutnohorite
814 from the Úrkút Mn-carbonate mineralization, Hungary. *Mineralogical Magazine* 71, 493–
815 508.

816 Poulton, S. W., Fralick, P. W., & Canfield, D. E. (2010). Spatial variability in oceanic redox
817 structure 1.8 billion years ago. *Nature Geoscience*, *3*(7), 486–490.

818 Préat, A., Bouton, P., Thiéblemont, D., Prian, J. P., Ndounze, S. S., & Delpomdor, F. (2011).
819 Paleoproterozoic high δ13C dolomites from the Lastoursville and Franceville basins (SE
820 Gabon): Stratigraphic and synsedimentary subsidence implications. *Precambrian*
821 *Research*, *189*(1–2), 212–228.

822 Prieto, M., Fernández-González, A., Putnis, A., & Fernández-Díaz, L. (1997). Nucleation,
823 growth, and zoning phenomena in crystallizing (Ba, Sr)CO_3, Ba(SO_4, CrO_4), (Ba, Sr)SO_4,
824 and (Cd,Ca)CO_3 solid solutions from aqueous solutions. *Geochimica et Cosmochimica*
825 *Acta*, 61(16), 3383-3397.

826 Purgstaller, B., Mavromatis, V., Immenhauser, A., & Dietzel, M. (2016). Transformation of
827 Mg-bearing amorphous calcium carbonate to Mg-calcite—In situ monitoring.
828 *Geochimica et Cosmochimica Acta*, 174, 180-195.

829 Purgstaller, B., Goetschl, K. E., & Mavromatis, V. (2019). Solubility investigations in the
830 amorphous calcium magnesium carbonate system. *CrystEngComm* 21, 155-164

831 Putnis, A. (2009). Mineral replacement reactions. *Reviews in Mineralogy and Geochemistry*,
832 70(1), 87-124.

833 Ren, M. (2025). Carbonate sedimentation and early diagenesis of the Doushantuo Formation,
834 South China: A window into the terminal Proterozoic. *Sedimentary Geology*, *479*,
835 106847.

836 Roy, S. Sedimentary manganese metallogenesis in response to the evolution of the Earth
837 system. Earth-Sci. Rev. 2006, 77, 273–305.

838 Robbins, L. J., Fakhraee, M., Smith, A. J. B., Bishop, B. A., Swanner, E. D., Peacock, C. L.,
839 Wang, C. Le, Planavsky, N. J., Reinhard, C. T., Crowe, S. A., & Lyons, T. W. (2023).
840 Manganese oxides, Earth surface oxygenation, and the rise of oxygenic photosynthesis. In
841 *Earth-Science Reviews* 239, 104368.

842 Rodriguez-Blanco, J. D., Shaw, S., & Benning, L. G. (2015). A route for the direct
843 crystallization of dolomite. *American Mineralogist*, 100(5-6), 1172-1181.

844 Rosenberg, P. E., & Foit Jr, F. F. (1979). The stability of dolomite in aqueous solution: An
845 experimental investigation at 25° to 275°C. *Geochimica et Cosmochimica Acta*, 43(6),
846 951-955.

847 Shang, H. (2023). Dichotomous effects of oxidative metabolisms: A theoretical perspective
848 on the dolomite problem. *Global and Planetary Change*, *222*, 104041.

Shannon, R. D. (1976). Revised effective ionic radii and systematic studies of interatomic distances in halides and chalcogenides. *Acta Crystallographica Section A*, 32(5), 751-767.

Slaughter, M., & Hill, R. J. (1991). The influence of organic matter in organogenic dolomite formation at various temperatures and pressures. *Journal of Sedimentary Research*, 61(2), 296-303.

Spinks, S. C., Sperling, E. A., Thorne, R. L., LaFountain, F., White, A. J. R., Armstrong, J., Woltering, M., & Tyler, I. M. (2023). Mesoproterozoic surface oxygenation accompanied major sedimentary manganese deposition at 1.4 and 1.1 Ga. *Geobiology*, *21*(1), 28–43.

Stacey, J., Hood, A. v. S., & Wallace, M. W. (2023). Persistent late Tonian shallow marine anoxia and euxinia. *Precambrian Research*, 397, 107207.

Stumm, W. and Morgan, J.J. (1996). Aquatic Chemistry, Chemical Equilibria and Rates in Natural Waters. 3rd Edition, John Wiley & Sons, Inc., New York.

Trichet, J., & Defarge, C. (1995). Non-biologically supported organomineralization. *Bulletin de l'Institut Océanographique de Monaco*, 14(2), 203-236.

Tordi, P., Ridi, F., Samorì, P., & Bonini, M. (2025). Cation-Alginate Complexes and Their Hydrogels: A Powerful Toolkit for the Development of Next-Generation Sustainable Functional Materials. Advanced Functional Materials35, 2416390.

Vandeginste, V., Snell, O., Hall, M. R., Steer, E., & Vandeginste, A. (2019). Acceleration of dolomitization by zinc in saline waters. *Nature Communications*, 10(1), 1851.

Van Tendeloo, G., Amelinckx, S. & De Fontaine, D. (1985) On the nature of the ‘short-range order’ in 1/2{hkl} alloys. *Acta Crystallographica Section B: Structural Science*, 41, 281–292.

Yan, H., Pi, D. H., Jiang, S. Y., Mao, J., Xu, L., Yang, X., Hao, W., Mänd, K., Li, L., Konhauser, K. O., & Robbins, L. J. (2022). Mineral paragenesis in Paleozoic manganese ore deposits: Depositional versus post-depositional formation processes. *Geochimica et Cosmochimica Acta*, *325*, 65–86. doi: 10.1016/j.gca.2022.03.030

Wang, D., Wallace, A.F., De Yoreo, J.J., Dove, P.M., 2009. Carboxylated molecules regulate magnesium content of amorphous calcium carbonates during calcification. *Proceedings of the National Academy of Sciences* 106, 21511–21516.

Wigley, T. (1973). The incongruent solution of dolomite. *Geochimica et Cosmochimica Acta,* 37, 1397-1402

Wilcots, J., Gilbert, P., & Bergmann, K. (2025). Nanoscale crystal fabric preserved in dolomite ooids at the onset of the Ediacaran Shuram excursion. *The Sedimentary Record,* 23 (1).

Wilkinson, B. H., & Algeo, T. J. (1989). Sedimentary carbonate record of calcium-magnesium cycling. *American Journal of Science*, 289(10), 1158-1194.

Wood, R., Bowyer, F., Penny, A., & Poulton, S. W. (2018). Did anoxia terminate Ediacaran benthic communities? Evidence from early diagenesis. *Precambrian Research*, *313*, 134–147.

Xu, L., Yu, W., Konhauser, K. O., Guo, H., Jin, S., Ma, P., & Du, Y. (2025). Genesis of manganese-rich deposits in the Mesoproterozoic Gaoyuzhuang Formation, North China: Implications for atmospheric redox state and early eukaryote evolution. *Palaeogeography, Palaeoclimatology, Palaeoecology*, *668*, 112924.

Zhang, F., Xu, H., Konishi, H., & Roden, E. E. (2012a). Polysaccharide catalyzed nucleation and growth of disordered dolomite: A potential precursor of sedimentary dolomite. *American Mineralogist*, 98(11-12), 2070-2076.

Zhang, F., Xu, H., Konishi, H., & Roden, E. E. (2012b). Dissolved sulfide-catalyzed precipitation of disordered dolomite: Implications for the formation mechanism of sedimentary dolomite. *Geochimica et Cosmochimica Acta, 97*, 148–165.

Zhang, F., Shen, S. zhong, Cui, Y., Lenton, T. M., Dahl, T. W., Zhang, H., Zheng, Q.F., Wang, W., Krainer, K., & Anbar, A. D. (2020). Two distinct episodes of marine anoxia during the Permian-Triassic crisis evidenced by uranium isotopes in marine dolostones. *Geochimica et Cosmochimica Acta*, *287*, 165–179.

FIGURES

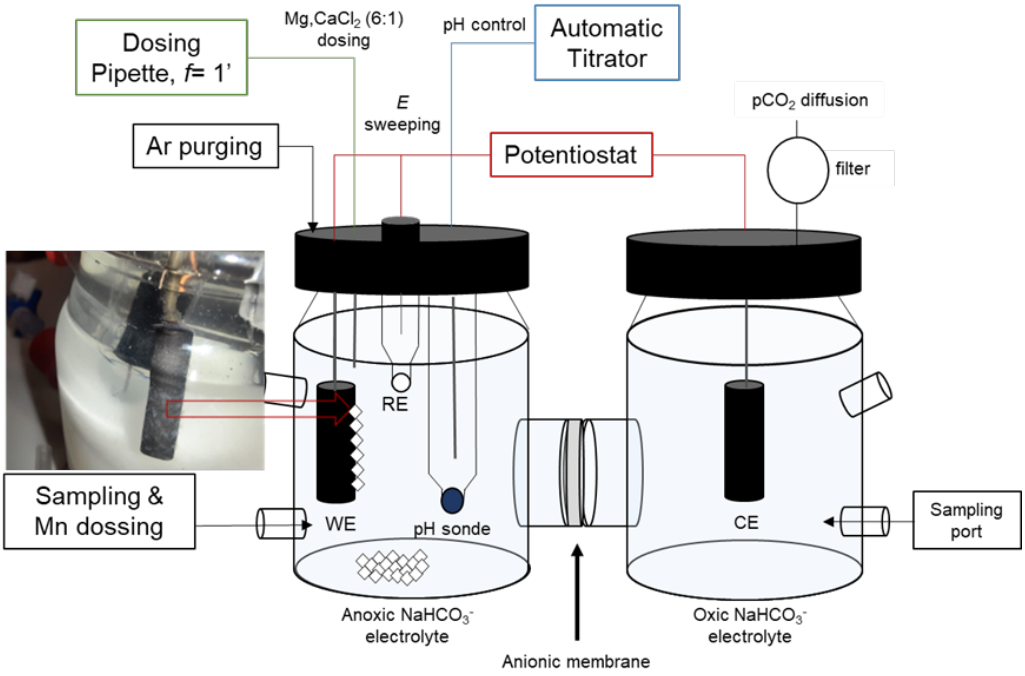

Figure 1. Schematic of the two-cell electrochemical precipitation apparatus. Two 150 mL borosilicate glass reaction vessels were connected via an anodic membrane. System hydrochemistry was controlled using an automatic pH-stat titrator and a potentiostat applying continuous potential sweeps. One cell, containing the working electrode (WE) and reference electrode (RE), was maintained under an Ar atmosphere, while the other, housing the counter electrode (CE), remained in equilibrium with air. Both WE and CE had surface areas of 4.2 $cm^{2.}$ The electrolyte consisted of $NaHCO_3$ solution. Following pre-titration (see test for details), the cation feedstock was introduced at 1' intervals using a dosing pipette (n=20); a single $MnCl_2$ dose was at t ~ 5' . The inset shows WE and surface precipitates, with residual precipitates formed quasi-instantaneously in solution upon reactant additions. Attention of this study is placed on the surface precipitates.

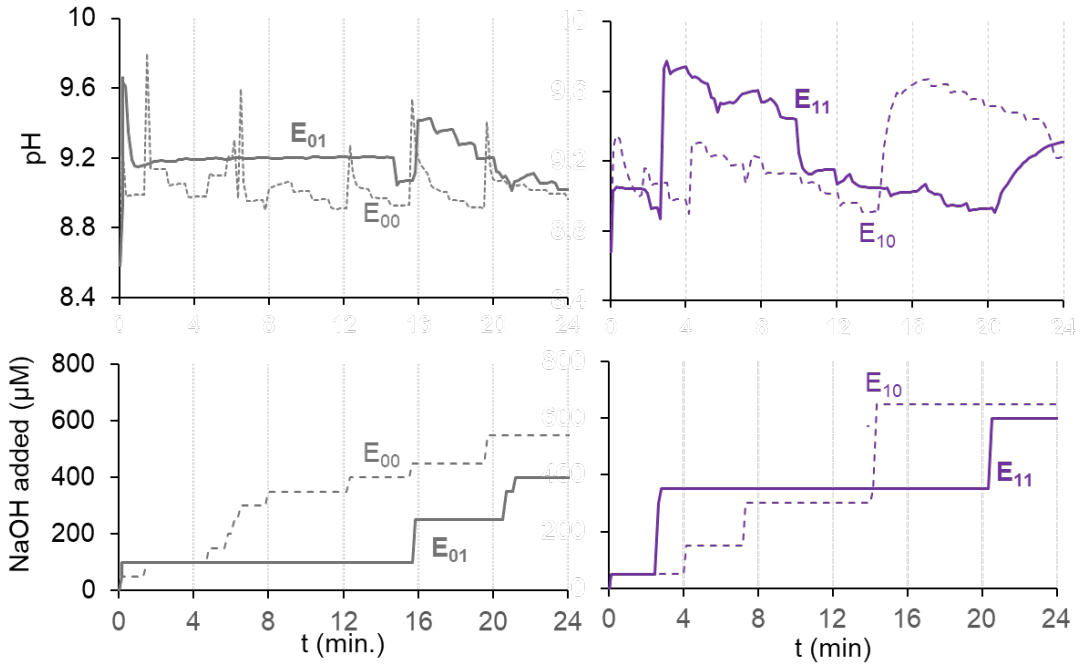

916

917 **Figure 2**. Experimental pH and NaOH additions during carbonate synthesis under four
918 conditions: control (E_{00}), electrochemistry only (E_{01}), functionalized only (E_{10}), and
919 combined (E_{11}). Electrochemistry and functionalization reduced titrant demand, enhancing
920 buffering.

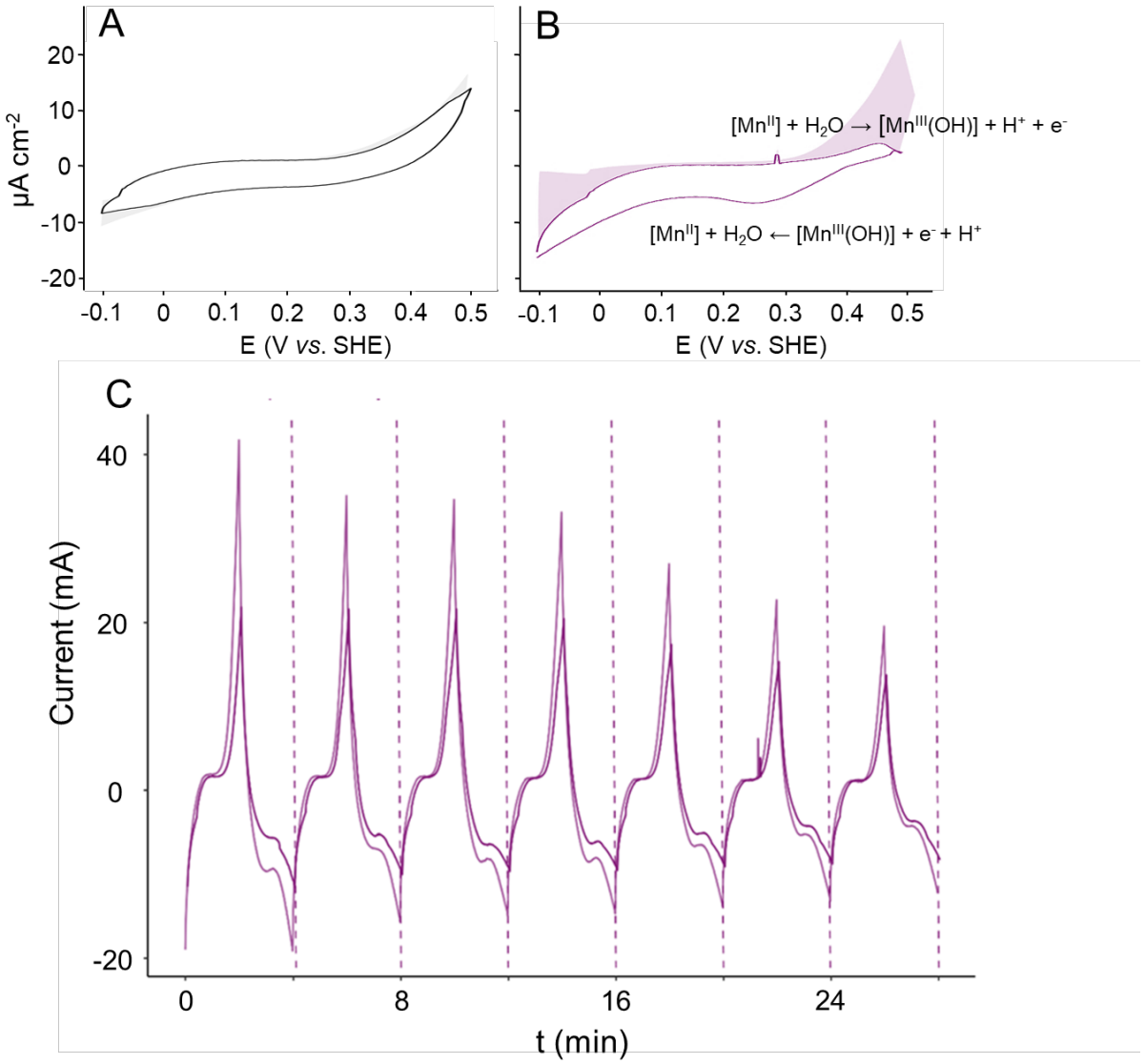

Figure 3. Electrochemical characterization of the Mn-functionalized system. Cyclic voltammograms (CV) recorded in carbonate-buffered electrolyte (E: [-0.1 to +0.5] V vs. SHE). (A) Control without functionalization exhibits a featureless profile characteristic of non-faradaic capacitive charging. (B) Carboxyl-functionalized hydrogel displays distinct quasi-reversible peaks, confirming active Mn redox cycling. Annotated equations detail the proposed proton-coupled electron transfer (PCET) mechanism: anodic oxidation coupled to hydrolysis (proton release) and cathodic reduction coupled to proton consumption. Solid lines denote average current density (j); shaded areas indicate standard deviation. (C) Temporal evolution of the current response (I) over 28 minutes in the functionalized system (E_{11}). Sharp peaks align with the 4-minute potential sweep periodicity (dashed lines). The progressive attenuation of peak intensity indicates gradual electrode passivation, consistent with the formation of non-conductive carbonate precipitate.

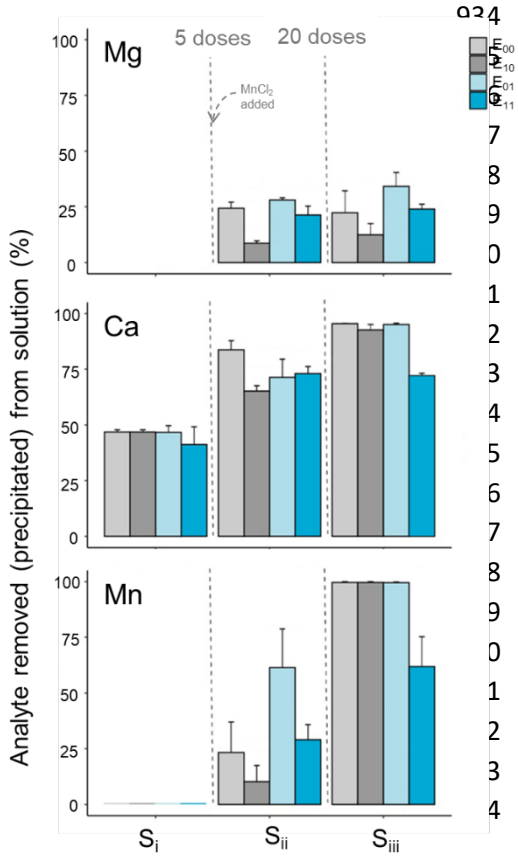

Figure 4. Percentage of Mg, Ca, and Mn removed (precipitated) from solution under four experimental conditions: without carboxyl groups (light grey), with carboxyl groups (dark grey), and their respective counterparts with electrochemical potential sweeping (light and dark blue). Samples were collected at three time points. These are S_i: 5' after start, with 5 doses of 1 mL $(Ca,Mg)Cl_2$ solution added to the system, and before the 10 mM $MnCl_2$ addition; S_{ii}: after 20', i.e., 20 doses of 1 mL of $(Ca,Mg)Cl_2$ solution; and S_{iii}: after the 24 h stabilization time lag. Consumption was calculated as the percentage difference between measured concentrations and maximum expected concentrations, i.e. @5' $\{[Mg]_{max}= 21$ mM, $[Ca]_{max}= 3.6$ mM, $[Mn]_{max}= 0.0$ mM$\}$; @20' and 24 h:$\{[Mg]_{max}= 86$ mM, $[Ca]_{max}= 14$ mM, $[Mn]_{max}= 10$ mM$\}$. Bars represent mean duplicate values, and whiskers indicate standard deviation based on duplicate experiments.

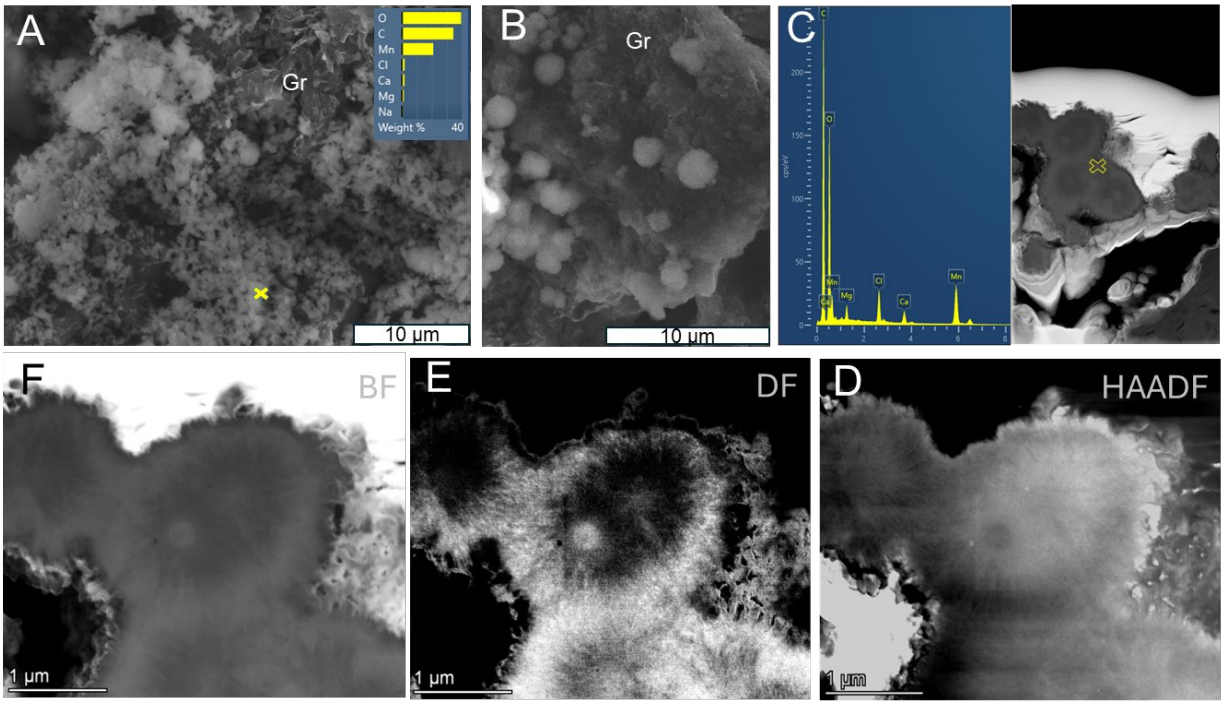

Figure 5. Solid phase characterization of carbonate precipitates in Control (E_{00}) vs. Functionalized (E_{10}) conditions. (A) SEM-EDS characterization of the control sample (E_{00}), where the absence of functionalization and cycling resulted in sparse, Mn-dominated precipitates (Mn >> Ca + Mg) with minimal surface accumulation. (B) SEM image of sample E_{10} (functionalization without electrochemical cycling), showing increased precipitate density and the formation of coherent carbonate spheroids on the graphite (Gr) substrate. (C) EDS spectrum of an E_{10} spheroid, confirming the phase as a manganous Mg-Ca carbonate. (D–F) Cross-sectional TEM analysis (HAADF, Dark Field, and Bright Field) of the E_{10} spheroids, revealing a spherulitic internal fabric composed of crystallites radiating outward from central nucleation centers.

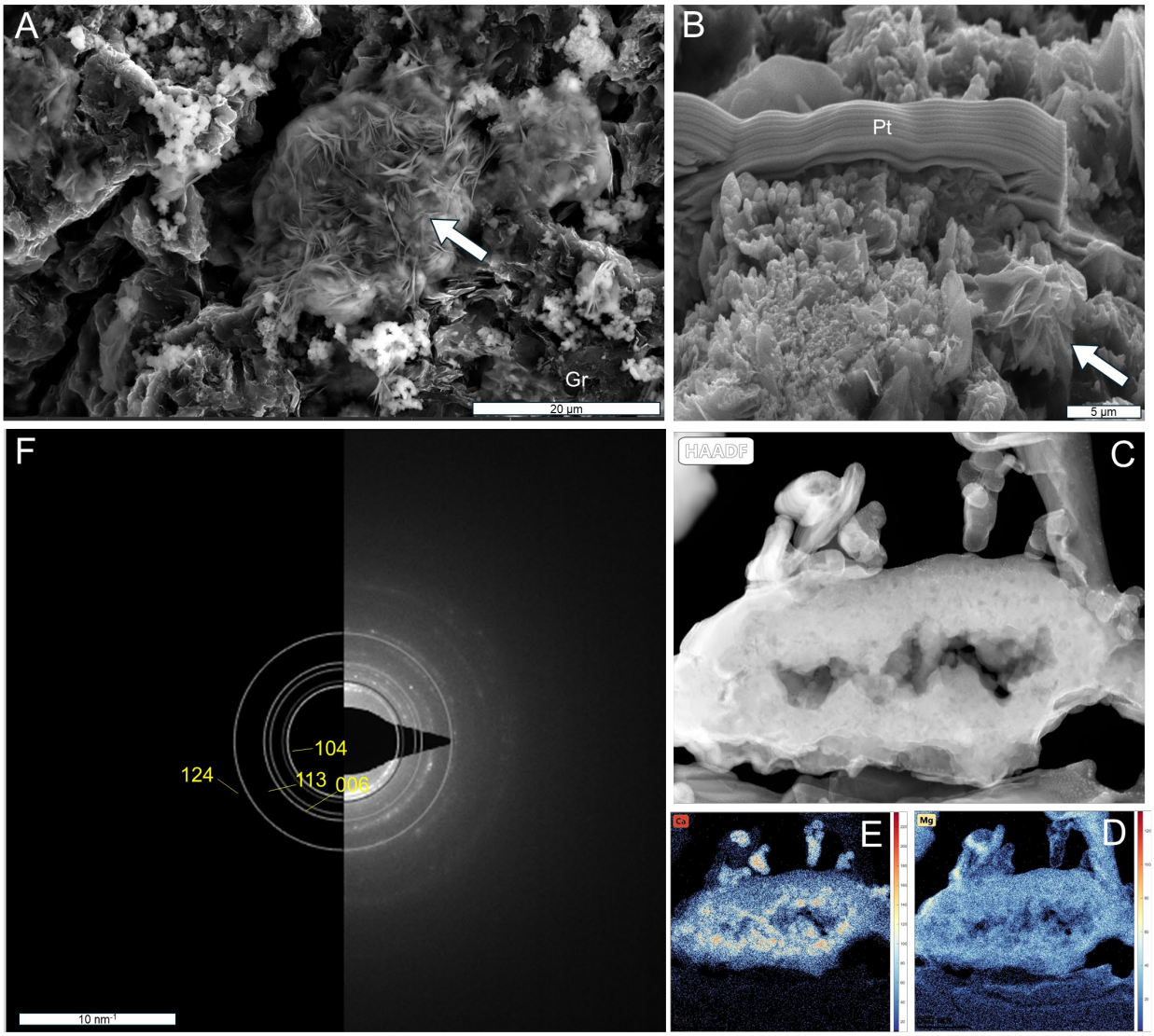

Figure 6. Morphology and structure of precipitates formed under electrochemical cycling without functionalization (E_{01}). (A) SEM of the electrode surface showing prominent rosette-like structures (arrow) intermixed with disperse, granular polycrystalline aggregates (B) FIB-milling site; the delicate rosettes (arrow) were unstable under the ion beam, leaving only the granular aggregates for analysis (C) STEM-HAADF cross-section revealing a porous, "vuggy" texture formed by coalesced nanocrystalline domains. Contrast variations highlight chemical zonation (inset mean EDS spectrum). (D–E) EDS maps contrasting the internal zonation of Ca with the homogeneously distributed Mg. (F) SAED pattern showing diffraction rings consistent with cation-substituted rhodochrosite lattice spacings.

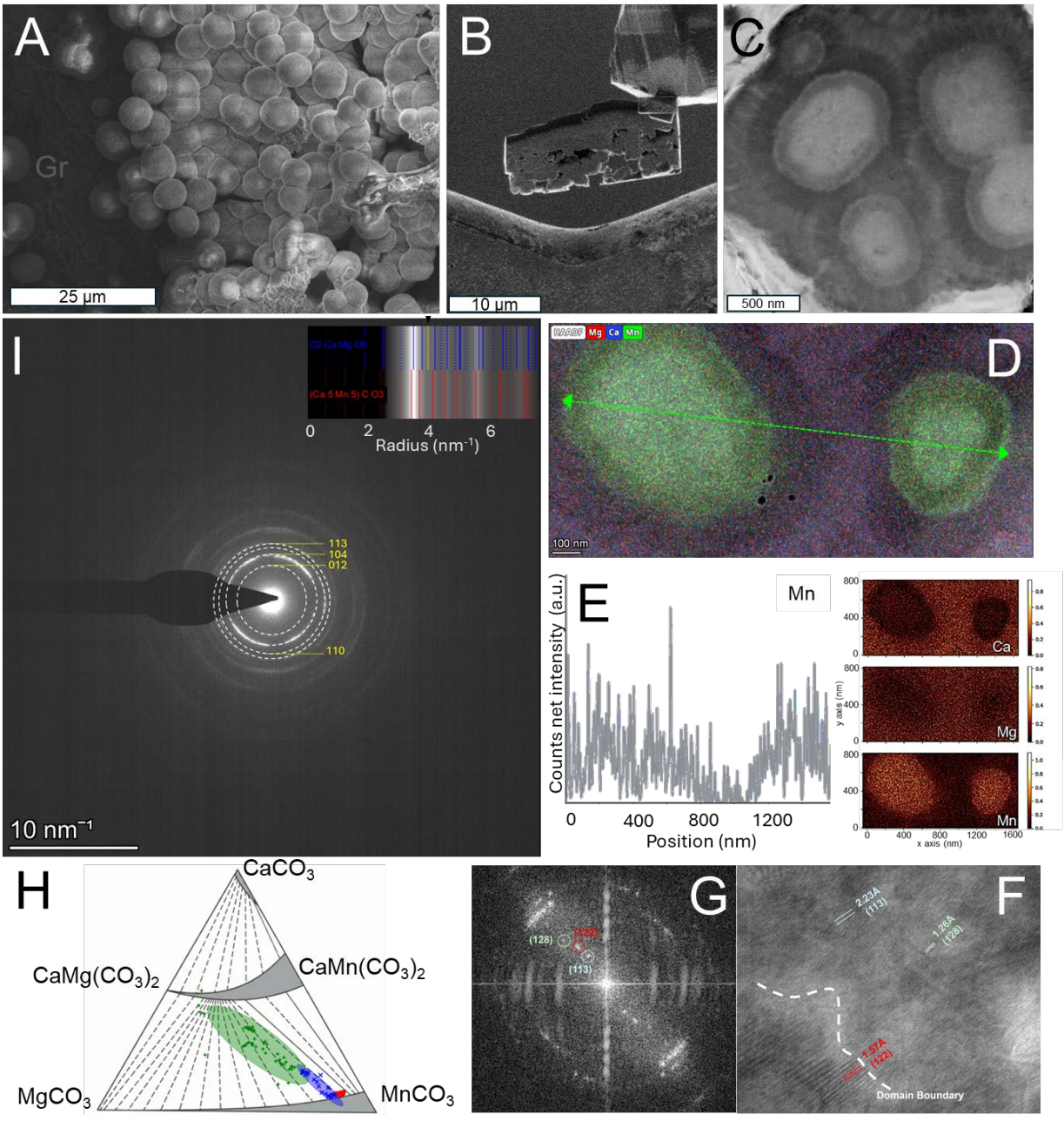

Figure 7. Multiscale characterization of Mn-templated protodolomite formed under electrochemical and carboxyl modulation (E_{11}). **(A–C) Morphology and texture: (A)** SEM micrograph showing the dense accumulation of spheroidal aggregates on the graphite electrode (Gr). **(B)** SEM view of a FIB-milled cross-section (lamella) extracted from the aggregate cluster. **(C)** STEM-HAADF image of the lamella, revealing the characteristic "eye-like" core-shell zonation and diverging sheaf texture. **(D–I) Nanostructure and chemistry**: **(D)** STEM-EDS composite map confirming cation partitioning: Mn-enriched cores (green) surrounded by Mg/Ca-rich cortices (red/blue). **(E)** EDS line-scan intensity profile (1.6 µm) for Mn across the aggregate (transect in D), showing the preferential sequestration of Mn in the core regions; the segregated distributions of Ca, Mg, and Fe are also shown. **(F)** High-resolution TEM (HRTEM) micrograph of a crystalline domain. The lattice fringes and the diffuse domain boundary (white dashed line) highlight the mosaic nanostructure, showing nanodomains (<30 nm) intergrowth together with different crystallographic orientations. **(G)**

Fast Fourier-Transform (FFT) of the HRTEM image **(H)** Compositional TEM-EDS data projected onto the $CaCO_3$-$MgCO_3$-$MnCO_3$ ternary plot, the low temperature two-phase manganoan carbonate stability fields/miscibility gap are shown (after Peacor et al.,1987). EDS data renormalized to [Ca] + [Mg] + [Fe] = 1. The confidence ellipses are calculated from the variance (scatter) of the data points. **(I)** SAED pattern acquired from the cortex with identified diffraction rings. The inset/overlay displays the theoretical ring positions for dolomite and kutnohorite, highlighting the expected location of the d_{015} superstructure reflection. This reflection may be highly attenuated by broadening and superposition of d_{104} peaks in polycrystalline matrices comprised of both minerals (see text for details).

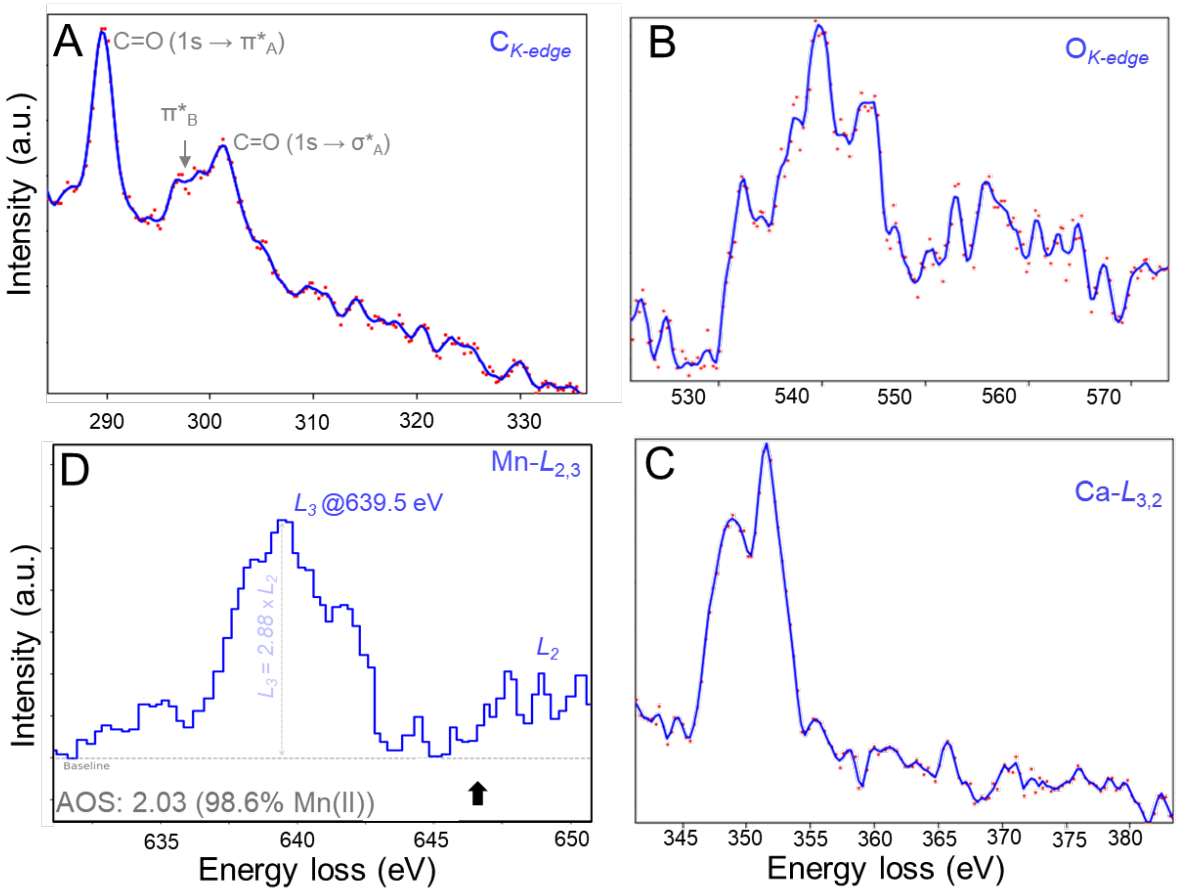

Figure 8. Representative core-loss EELS spectra acquired from the inner cortex region. (A) Carbon K-edge showing the characteristic π∗ and σ∗ transitions of the carbonate. (B) Oxygen K-edge exhibiting fine structure consistent with carbonate bonding. (C) Calcium $L_{3,2}$ -edge displaying sharp white lines indicative of a crystalline coordination environment. (D) Manganese $L_{2,3}$ edge spectrum. The data is presented as a raw step plot to preserve peak shape fidelity. The analysis reveals a sharp L_3 maximum at 639.5 eV and an intensity ratio of $L_3/L_2 \approx 2.88$, consistent with high-spin Mn(II). A key feature is the complete return to baseline intensity in the inter-peak valley (~645 eV, black arrow), effectively ruling out significant mixed-valence contributions.

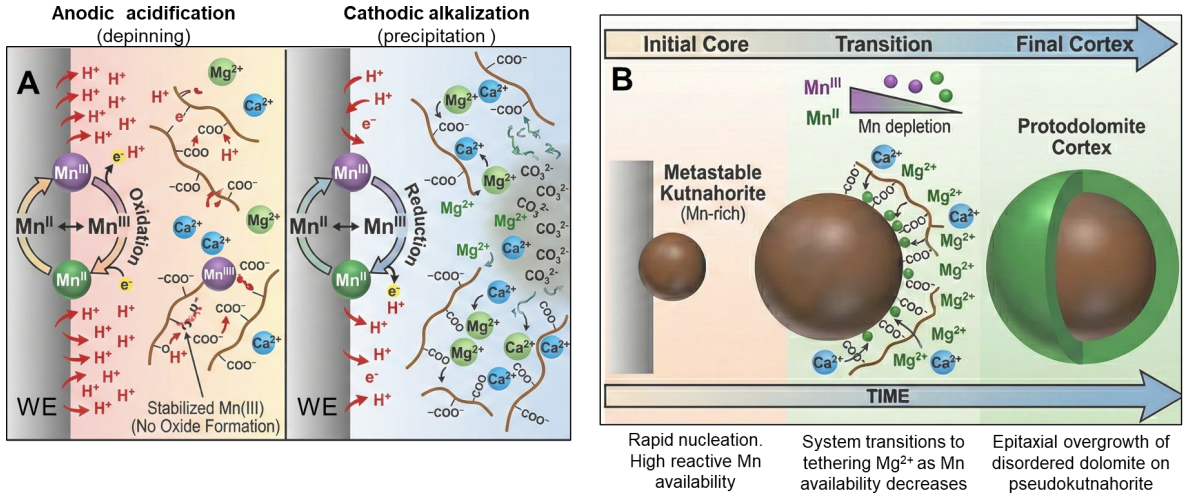

Fig. 9. Proposed mechanism of electrochemically induced dolomite growth. (A) The proton-coupled redox engine. At the working-electrode interface, anodic oxidation of Mn and concurrent water splitting generate Mn and protons (H^+). This drives anodic acidification, in the vicinity of the electrode which transiently protonates alginate ligands and causes the depinning of bound cations (Mg^{2+}, Ca^{2+}). The subsequent cathodic alkalization consumes protons, reactivating the ligands to bind cations and producing a local supersaturation spike. The carboxyl ligands form stabilized Mn complexes, acting as a kinetic brake that prevents oxide formation and sustains the quasi-reversible cycle. (B) Core-to-cortex evolution. Initially high concentrations of reactive Mn drive the rapid nucleation of a pseudo-kutnahorite template. As aqueous Mn availability progressively decreases (see transition wedge), the pumping mechanism shifts toward tethering the increasingly abundant Mg ions. These are delivered to the growth front, facilitating the epitaxial overgrowth of a protodolomite cortex.

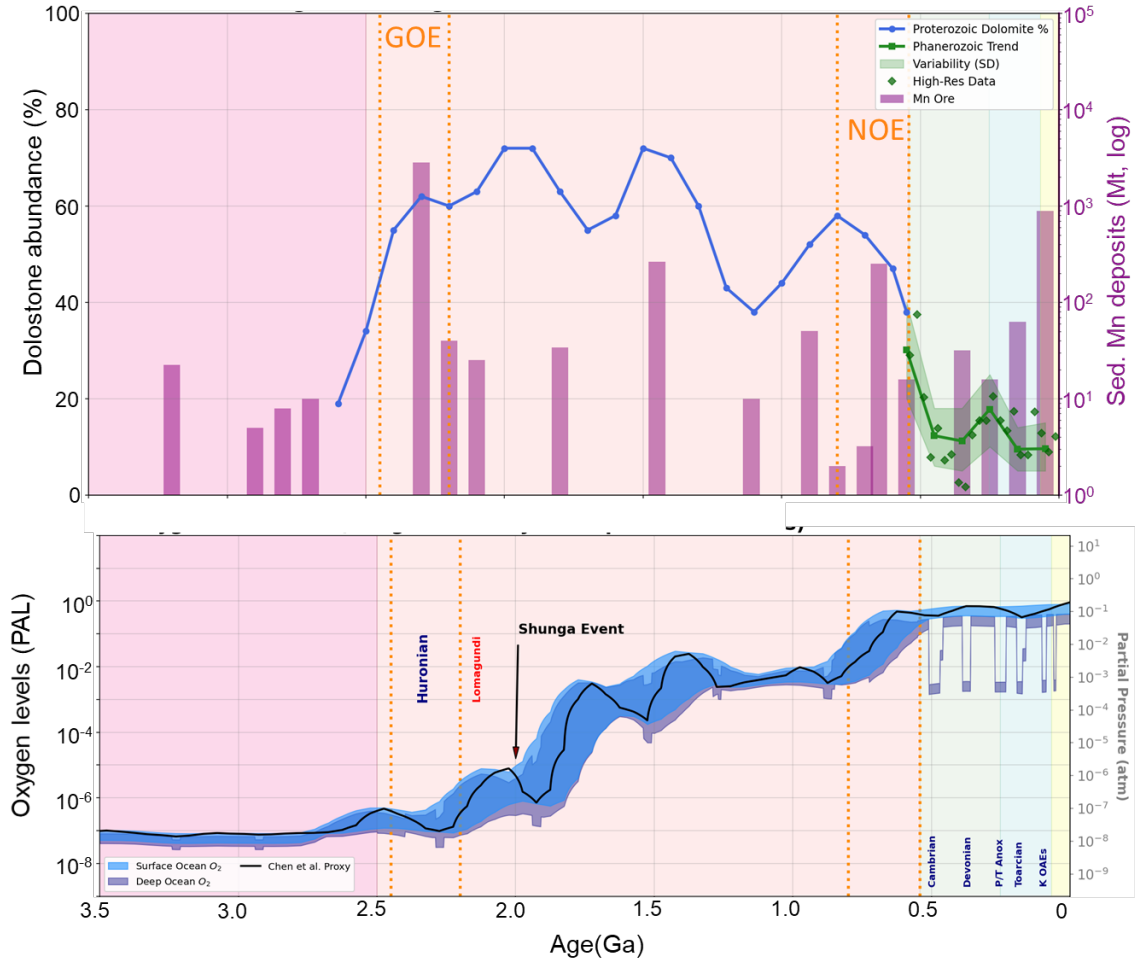

Figure. 10 Integrated evolution of global ocean redox conditions, carbonate mineralogy, and manganese deposition. (A) Secular trends in dolomite abundance (blue: Proterozoic; green: Phanerozoic mean ± SD; derived from Shang et al., 2023; Li et al., 2021) plotted against Mn ore deposits (purple bars; Robbins et al., 2023). Note the strong co-occurrence of dolomite peaks with Mn pulses in the Precambrian. (B) Evolution of oxygenation states (pO_2). Surface envelopes are calibrated to Chen et al. (2022). The deep ocean tracks surface conditions in the Mesoproterozoic but decouples during high-amplitude redox fluctuations: (i) the Great Oxidation Event (GOE) and Huronian glaciations; (ii) the Lomagundi-Jatuli overshoot; (iii) the Shunga Event oxygen crash; and (iv) the Neoproterozoic Oxygenation Event (NOE). In the Phanerozoic, the deep-water "Mn-pump" is largely suppressed, re-emerging only during transient Ocean Anoxic Events (e.g., P-Tr, Toarcian, K-OAEs) where deep waters dropped to <1% surface saturation.

TABLE

Table S1. Summary of aqueous geochemical evolution and cation removal efficiencies.

Parameter	Initial Phase (Doses 1–5)	End of titration (20 doses)[†] [‡]	Stabilization 24h[†]	Primary controlling factors
NaOH Titrant	**Delayed onset:** Lag in consumption (0–15 min) due to proton consumption from Mn(III) reduction	**Linear increase:** Steady demand to buffer proton release from precipitation	**Converged:** Total volume ~ 0.50–0.60 mL (0.25–0.30 mmol-eq OH^-) across all experiments.	Proton consumption by electrochemical Mn-reduction vs. alkalinity demand from carbonate equilibrium ($HCO_3^- \rightarrow CO_3^{2-} + H^+$)
Mg removal	**Negligible:** No significant uptake observed.	**Variable:** 8.7 ± 1.1 % (E_{10}) to 28.0 ± 1.0% (E_{01}). Highest in electrochemical setups, but reduced by carboxyl (E_{11} < E_{01})	**Incomplete:** Slight increase (3-6%). Majority (66-87%) persists in solution.	Electrochemical treatment enhances Mg co-precipitation, but carboxyl functionalization partially mitigates this effect
Ca removal	**Rapid:** >40% removal prior to Mn addition (ACC formation)	**High:** 65.2 ± 2.4% to 83.7 ± 4.1% removal	**Near complete:** >95% removal, except E_{11} (~75%)	Initial homogeneous nucleation of ACC ; partially inhibited by ligand stabilization in E_{11}.
Mn removal	**N/A:** Mn added after Dose 5.	**Kinetic Response:** $E_{01} \gg E_{00}$, w./ E_{01} (61.4%) > E_{11} (29.0%) > E_{00} (23.3%) > E_{10} (10.2%)	**Complete vs. stabilized:** >99% removal in most units. Exception: E_{11} retains 25-38% in solution	Applied potential drives rapid sequestration; alginate in E_{11} stabilizes Mn(III) intermediates against precipitation

[†] Conditions denote E_{00} (control), E_{01} (electrochemistry only), E_{10} (functionalized only), and E_{11} (combined).
[‡] Removal (%)calculated relative to the total molar mass added to the H-cell reactor.

SUPPLEMENTARY MATERIAL

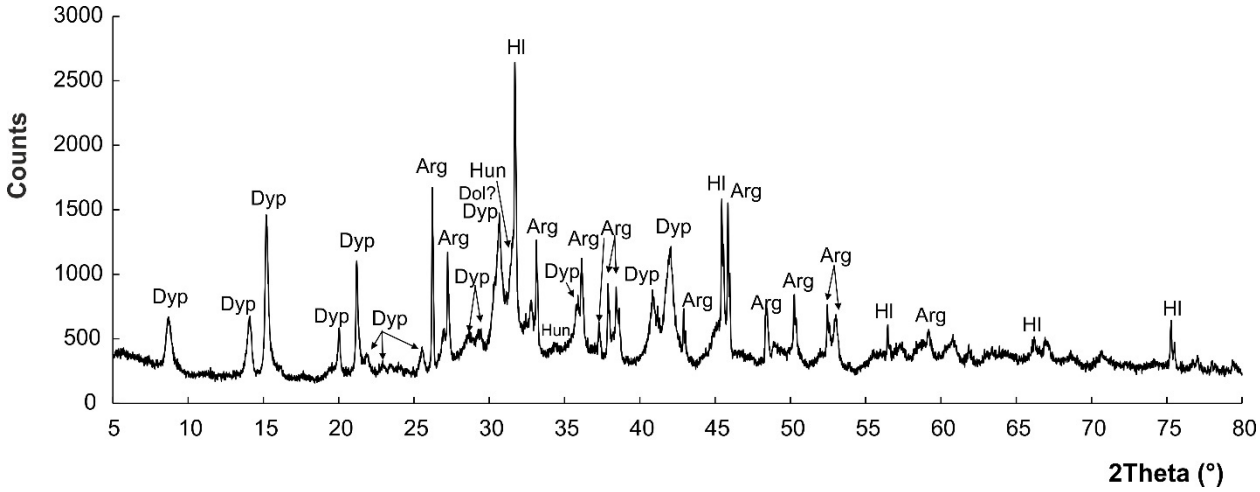

Fig. S1. 1-D X-ray diffraction pattern of the residual solid phase. The mineral assemblage was analyzed after complete evaporation of the parental H-cell solution at 25 °C. Identified phases include aragonite (Arg), dypingite, $Mg_5(CO3)_4(OH)_2 \cdot 5H_2O$ (Dyp), and halite. (Dyp) and halite.

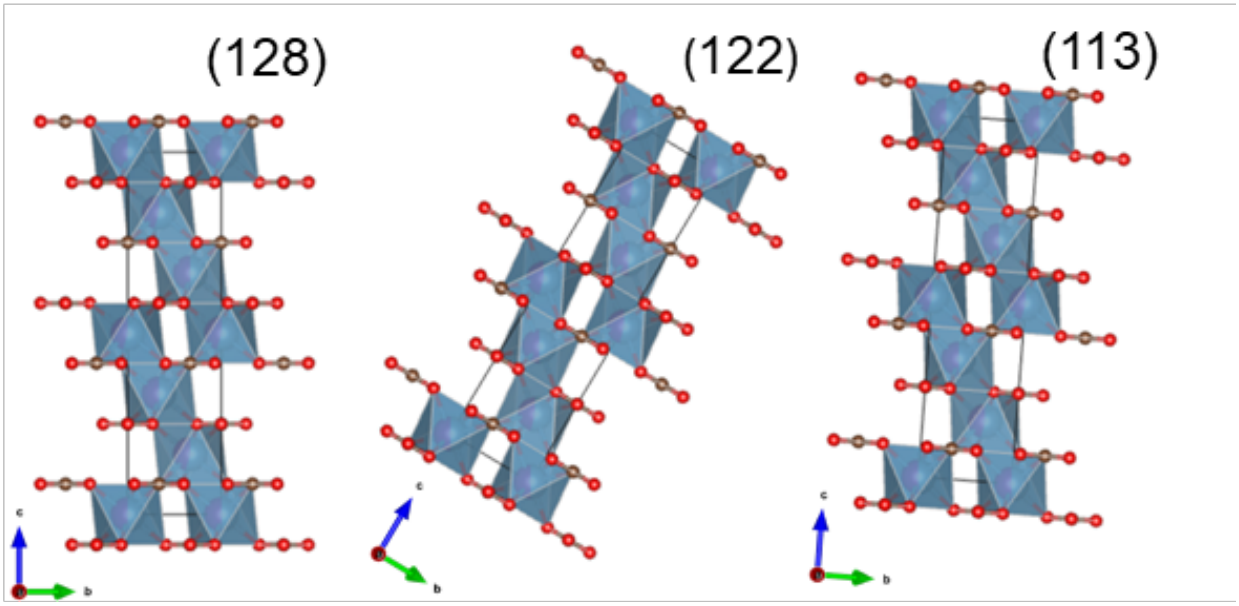

Figure S2 | Fast Fourier Transform (FFT) generated from the HRTEM micrograph in Figure 7F. The pattern displays discrete diffraction spots corresponding to the (128), (122), and (113) lattice planes. The characteristic arcing of these spots highlights the rotational mismatch between adjacent nanodomains, quantifying the crystallographic misorientations (~3 to 11º) associated with the mosaic fabric.

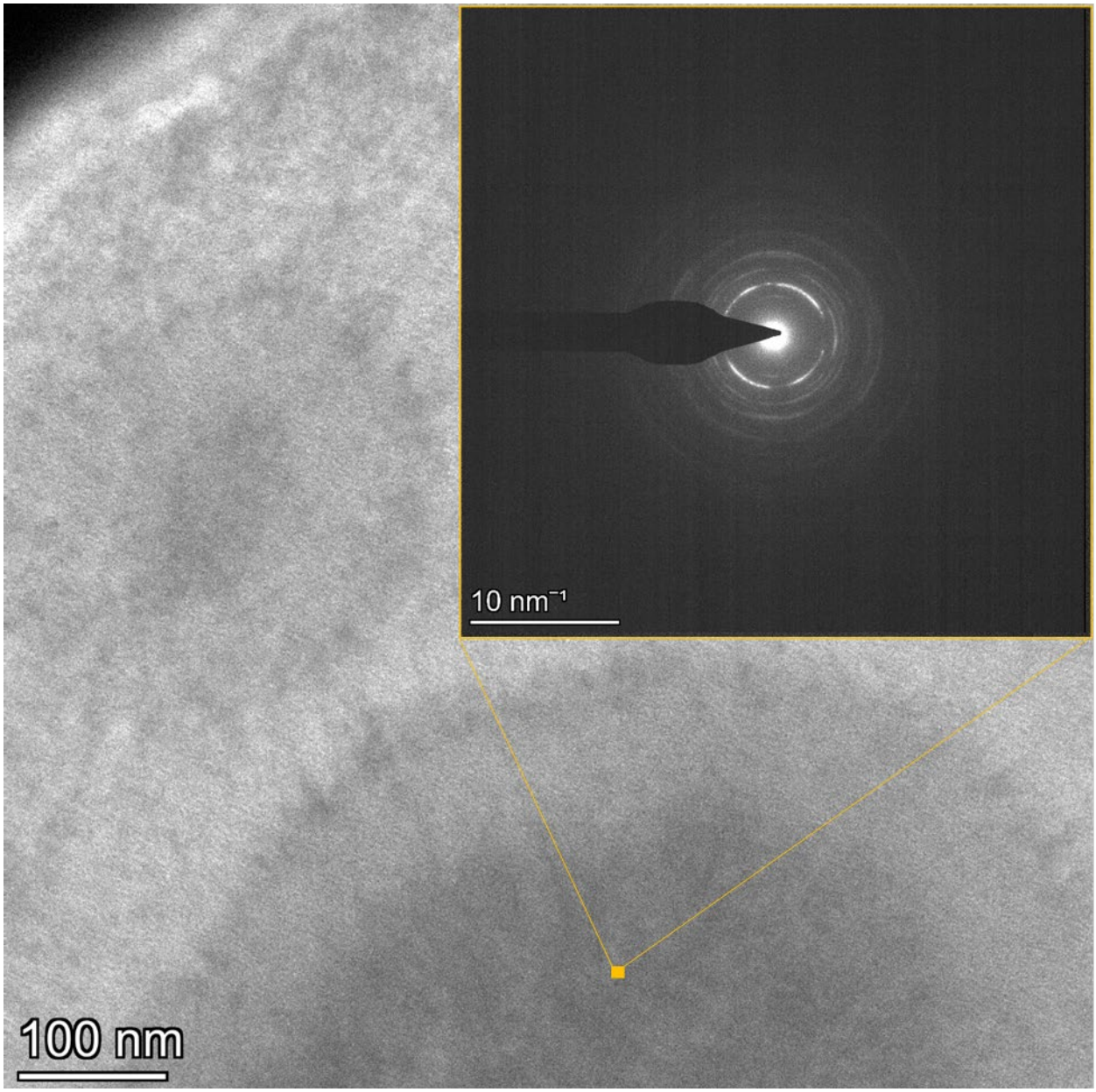

Figure S3. Selected-area electron diffraction (SAED) pattern (inset) acquired from the core of one of the spheroidal features resulting from E_{11}. The diffraction geometry is consistent with kutnaharite, based on estimation analyses using AMCSD entry 0001070 (after Peacor et al. 1987).

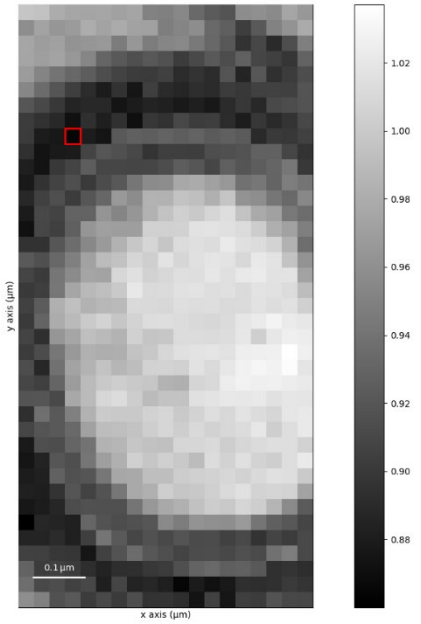

Figure S4. $t(\lambda)^{-1}$ map across a spheroidal ROI. Derived from the low-loss electron energy loss spectra (Malis et al., 1988), the map displays the spatial variation in sample thickness relative to the inelastic mean free path, $t(\lambda)^{-1}$. The darker grey regions correspond to the Mg-rich cortices (e.g., red square), while the bright central regions correspond to the thicker Mn-rich cores ($t(\lambda)^{-1} \approx 1.02$). In this regime ($(\lambda)^{-1} > 0.5$), inelastic scattering significantly contributes to the background signal (unscattered fraction = e^-$t(\lambda)^{-1} \approx 0.41$, i.e., 41% of the beam is coherent (unscattered). The other 59% creates inelastic background noise, which hinders the detection of weak diffraction intensities such as the cation ordering (b-type) superlattice reflections. Calculated using HyperSpy (https://doi.org/10.5281/zenodo.14956374).

Malis, T., Cheng, S. C., & Egerton, R. F. (1988). EELS log-ratio technique for specimen-thickness measurement in the TEM. *Journal of Electron Microscopy Technique*, 8(2), 193–200

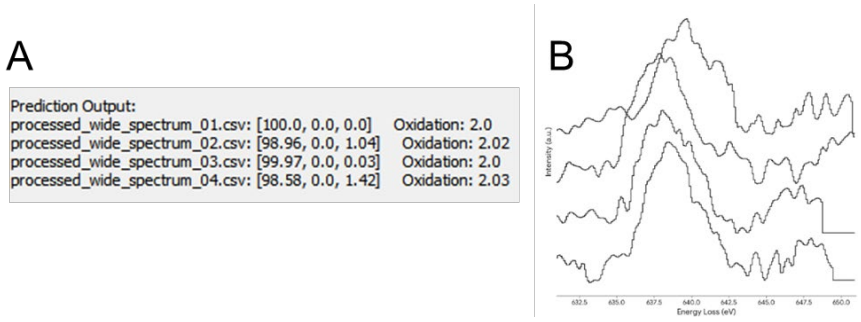

Figure S5. Results of the model MnEdgeNet (https://github.com/xinhuolin/MnEdgeNet/tree/main 5). Stacked raw EELS spectra of the Mn $L_{2,3}$-edge acquired from four representative locations within the spheroid core (range 631–651 eV). Vertical offsets are applied for clarity. All scans consistently display a sharp L_3 absorption maximum at 693.5 to 640.0 eV and a deep inter-peak valley returning to baseline intensity. These identical spectral features confirm the spatial homogeneity of the pure high-spin Mn(II) oxidation state across the analyzed region.

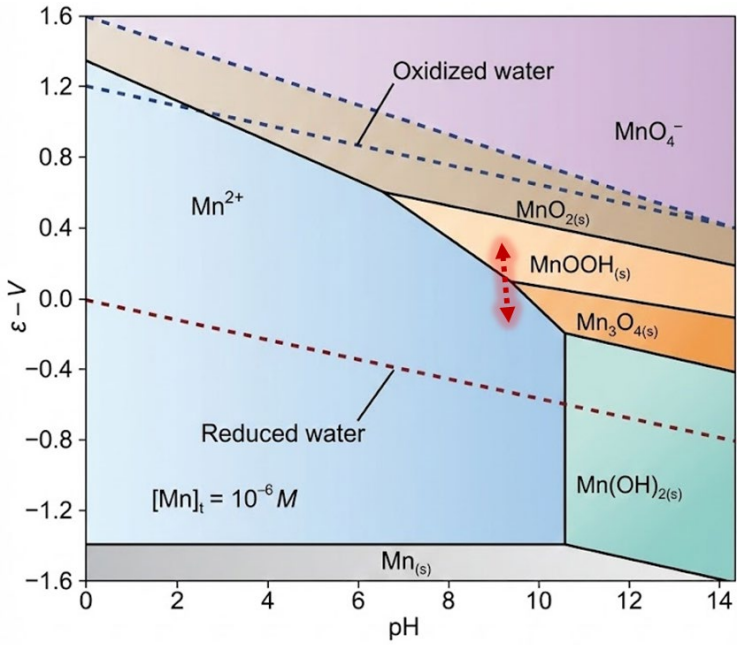

Figure S6. Eh-pH stability diagram for the Mn water system at 25°C. The diagram plots redox potential (ε–V) against acidity (pH), showing the thermodynamically stable fields for various manganese species at a total manganese molar concentration of [Mn]t = 10^{-6} M. Solid lines delimit the stability boundaries between species. Aqueous species shown are the manganous ion (Mn^{2+}) and permanganate (MnO_4^-). Solid phases, denoted by the subscript (s) and distinct color shading, include pyrochroite ($Mn(OH)_2(s)$), hausmannite ($Mn_3O_4(s)$), manganite (MnOOH(s)), and pyrolusite ($MnO_2(s)$). Adapted from Faust & Aly (1998) and Stumm & Morgan (1996). The approximate experimental trajectory is shown (arrow)

Table S1. Saturation state of relevant mineral phases in the functionalized active electrolyte (E_{11}). Values represent the Saturation Index (SI = log(IAP) - log(K)) calculated for the mixture composition S_{ii}. Positive SI values (>0) indicate supersaturation, while negative values (<0) indicate undersaturation. Note that the S_{ii} is strongly supersaturated with respect to aragonite, dolomite, and hydromagnesite, consistent with the observed mineral assemblage.

Phase	SI	logIAP	logK	Formula
Huntite	8.81	-21.15	-29.97	$CaMg_3(CO_3)_4$
Dolomite	6.09	-11	-17.09	$CaMg(CO_3)_2$
Dolomite(d)	5.54	-11	-16.54	$CaMg(CO_3)_2$
Hydromagnesite	5.01	-3.75	-8.76	$Mg_5(CO_3)_{4(}OH)_2 \cdot 4H_2O$
Rhodochrosite	4.18	-6.95	-11.13	$MnCO_3$
Rhodochrosite(d)	3.44	-6.95	-10.39	$MnCO_3$
Magnesite	2.95	-5.08	-8.03	$MgCO_3$
Calcite	2.55	-5.93	-8.48	$CaCO_3$
Aragonite	2.41	-5.93	-8.34	$CaCO_3$
Artinite	1.88	11.48	9.6	$MgCO_3$:$Mg(OH)_2$:$3H_2O$
Nesquehonite	0.54	-5.09	-5.62	$MgCO_3$:$3H_2O$
Pseudo-kutnahorite†	-2.57	-12.87	-10.3	$MnCa(CO_3)_2$
Nahcolite	-3.12	-3.67	-0.55	$NaHCO_3$
Natron	-5.06	-6.37	-1.31	Na_2CO_3:$10H_2O$
Thermonatrite	-6.47	-6.35	0.12	Na_2CO_3:H_2O
Trona	-9.23	-10.02	-0.8	NaHCO3:Na2CO3:$2H_2O$
Pyrochroite	-0.5	14.7	15.2	$Mn(OH)_2$
Brucite	-0.27	16.57	16.84	$Mg(OH)_2$
Portlandite	-7.08	15.72	22.8	$Ca(OH)_2$
Manganite	-5.11	20.23	25.34	MnOOH
Hausmannite	-5.87	55.16	61.03	Mn_3O4
Bixbyite	-9.96	-10.57	-0.61	Mn_2O_3
$MnCl_2 \cdot 4H_2O$	-7.87	-5.16	2.71	$MnCl_2 \cdot 4H_2O$

Notes: Calculations were performed using the U.S. Geological Survey geochemical code PHREEQC (Parkhurst and Appelo, 2013) employing the wateq4f thermodynamic database. (d) denotes disordered or metastable phases included in the database. † Solubility product (log K_{sp}) for pseudokutnahorite is adapted from Mucci (2004). Data Availability: The input code and full dataset for these calculations are available in the Zenodo repository (see Data Availability Statement).

Supplementary Note S1: Estimation of local interfacial pH and saturation state of dolomite near the electrode-mineral interface

1. Model assumptions

To estimate the magnitude of pH oscillations at the working electrode (WE) surface, we apply a simplified steady-state Nernst-Planck approximation. The model assumes a stagnant diffusion boundary layer (Nernst diffusion layer, Δ) separating the electrode surface from the bulk electrolyte.

We adopt the following governing assumptions:

1. Transport control: mass transport of protons (H^+) and reactants is governed primarily by diffusion across the boundary layer; migration effects are minimized by the supporting electrolyte.
2. Stoichiometry: the anodic oxidation of Mn(II) to Mn(III) coupled with hydrolysis generates protons. We conservatively assume a localized proton flux (J_{H+}) proportional to the measured current density (j).
3. Layer thickness: For an unstirred vertical electrode under natural convection, Δ is estimated at *ca.* 200 μm (2×10^{-2} cm) (Bard & Faulkner, 2001).
4. Bulk conditions: Bulk solution is maintained at pH 9.1 (experimental baseline).

2. Flux Calculation

The J_{H+} generated at the anode is derived from Faraday's Law:

$J_{H+} = j(nF)^{-1}$

Where:

- $j \approx 100$ μA cm^{-2} (T_{peak} current density observed in CV scans).
- n = 1 (electrons transferred per proton equivalent).
- F = 96,485 C mol^{-1} (Faraday constant).

$J_{H+} = 10^{-4}$ (96485)= 1.04×10^{-9} mol cm^{-2} s^{-1}

3. Interfacial pH shift

According to Fick's First Law, the concentration gradient (ΔC) required to sustain this flux across layer Δ is:

$$\Delta H^+ \approx J_{H+} \times \delta \, (D_H)^{-1},$$

where:

- $D_H \approx 9.3 \times 10^{-5}$ cm^2 s^{-1} (diffusion coefficient of H^+ in water at 25°C).
- $\delta \approx 0.02$ cm

$\Delta H^+ \approx 1.04 \times 10^{-9}\,(0.02)/(9.3 \times 10^{-5}) \approx 2.21\ 10^{-7}$ M

Resulting surface pH: the bulk proton concentration at pH 9.1 is $[H^+]_{bulk} \approx 7.9 \times 10^{-10}$ M.

The surface concentration $[H^+]_{surf}$ is the sum of the bulk concentration and the anodic accumulation $\Delta[H^+]$):

$$[H^+]_{surf} \approx 7.9 \times 10^{-10} + 2.2 \times 10^{-7} \approx 2.21 \times 10^{-7} \text{ M}$$

$$\underline{pH_{surf} = -\log(2.21 \times 10^{-7}) \approx 6.65}$$

The unbuffered anodic shift is $\Delta pH \approx -2.45$ units. However, in the presence of the (bi)carbonate/alginate buffering system, this theoretical drop can be substantially attenuated (see Fig. 2). Conservatively estimating a 50–70% buffering efficiency, then the effective localized shift is $\Delta pH \approx \pm 0.5$ to 1.2 units.

4. Impact on supersaturation (SI_{dol})

The saturation state for dolomite (SI_{dol}) is defined as:

$$SI_{dol} = \{Ca^{2+}\}\{Mg^{2+}\}\{CO_3^{2-}\}^2 K_{sp}^{-1}$$

Since CO_3^{2-} is strictly pH-dependent, the calculated anodic acidification near the WE surface (pH 9.1 to ~8.0 to 8.5) causes a logarithmic decrease in local carbonate ion activity.

- Anodic phase (oxidation): local pH drops, SI_{dol} decreases significantly (undersaturation or low supersaturation), promoting the dissolution of kinetic defects.
- Cathodic phase (reduction): local pH is restored or increased (via proton consumption), SI_{dol}, driving rapid nucleation.

This confirms that electrochemical cycling imposes a high amplitude oscillation of the saturation state (SI_{dol}), mimicking the Ostwald ripening mechanism required for ordering.

5. Scan rate justification: The electrochemical experiments utilized a fixed scan rate of 10 mV s^{-1}. This rate was selected to establish a stable diffusion profile (δ) that balances the anodic proton production with the buffering capacity of the hydrogel, creating a sustained, reproducible saturation gradient necessary for crystal growth.

References

Bard, A. J., & Faulkner, L. R. (2001). *Electrochemical Methods: Fundamentals and Applications*. Wiley.

Stumm, W., & Morgan, J. J. (1996). *Aquatic Chemistry*. Wiley-Interscience.

Supplementary Note S2. A working-table compiling sedimentary units of interest to test the mechanism proposed in the main text. Have fun.

Period	Formation / Location	Dominant Texture & Key Features	References*
Holocene	Sabkha Flats (Al Jubayl, Saudi Arabia)	Microbial mats; Quaternary ordered dolomite.	(C'hafetz et al., 1999)
Holocene	Sabkha Flats (Abu Dhabi/Qatar)	Microbial mats; protodolomite forming in EPS-rich layers; seasonal cycling.	(Bontognali et al., 2010; Di Loreto et al., 2021)
Holocene	Lake Van (Turkey)	Cyclic early diagenetic dolomite; triggered by hydrochemical mixing and redox perturbations.	(McCormack et al., 2018, 2024)
Miocene	Eger Rift Paleolake (Czech Rep.)	Episodic carbonate cementation driven by Mn–N redox cycling in a non-marine setting.	(Petrash et al., 2025)
Eocene	Green River Formation (USA)	Lacustrine dolomite; vast deposits formed in organic-rich, stratified (meromictic) alkaline paleolakes.	(Pommer et al., 2023)
Triassic (Ladinian)	Dolomite Mtns / Sella Group (Italy)	The "Dolomite" Archetype. synsedimentary	Meister et al., 2013), Sedimentology 60(1):270-291
Permian-Triassic	Inner Platform (Dinarides, Croatia)	Dolomitization linked to oceanic anoxia and chemocline shifts; inner platform facies.	(Aljinović et al., 2025)
Devonian	Ratner Formation (Canada, SK)	Partially recrystallized medium-sized dolomite with high. Mn contents (ME)	Fu & Qinq, 2010, *Carbonates and Evaporites* 26, 111-115
Devonian	Grosmont Formation (Canada, AB)	Sabkha dolomite forming within burrowed stromatolites; microbial influence.	(Baniak et al., 2014)
Upper Cambrian (Furongian)	Chaomidian Fm. (North China Platform)	Fabric-retentive microbial dolomite; thrombolite-stromatolite reefs	(Han et al., 2024; Chen et al., 2014)

Period	Formation / Location	Dominant Texture & Key Features	References*
Lower Cambrian	Xiaoerbulake Fm. (Tarim Basin, China)	Fabric-retentive dolomicrite; microbialites (stromatolites/thrombolites).	(Zhang et al., 2022; Zheng et al., 2022)
Ediacaran (Shuram Excursion)	Khufai, Buah & Birba Fms (Oman)	Primary Nanoscale Fabrics; fibrous dolomite ooids, spherulitic stromatolites, and fibrous cements.	(Wilcots et al., 2025)
Ediacaran	Doushantuo Formation (China)	Cap dolostone featuring interlinked cycles of methane, manganese, and sulfate.	(Cai et al., 2023)
Mesoproterozoic (~1.6 Ga)	McArthur Basin (Amelia/Mara Dol.), Australia	Massive fabric-retentive dolostone; Mn-mineralized sheaths; exceptional eukaryotic cell preservation.	(Muir, 1976, 1983)
Mesoproterozoic (~1.6 Ga)	Chuanlinggou Formation, N China	Fabric retentive. Mn-bearing dolomitic siltstone	(Xu et al., 2025)
Mesoproterozoic (~1.5 Ga)	Gaoyuzhuang Formation, N China	Syndiagenetic, consist of dolommicrite, along with kutnohorite and rhodochrosite	(Xu et al., 2025)
Mesoproterozoic (~1.4–1.1 Ga)	Bangemall Supergroup (W. Australia)	Sizable Mn deposits associated with surface oxygenation events.	(Spinks et al., 2023)
Paleoproterozoic (~2.1 Ga)	Francevillian Succession (Gabon)	Intimate association Mn-Ca carbonate	(Nzamba et al., 2026; Préat et al., 2011)

1192 * (Refer to the main text). Unless otherwise indicated.